ALMA MATER STUDIORUM — UNIVERSITÀ DI BOLOGNA

SCUOLA DI SCIENZE

Dipartimento di Chimica Industriale "Toso Montanari"

Corso di Laurea Magistrale in

Chimica Industriale

Classe LM-71 - Scienze e Tecnologie della Chimica Industriale

A 2-pyridyl-2,1-borazaronaphthalene derivative as forefather of a new class of bidentate ligands: synthesis and application in luminescent Ir(III) complexes

Tesi di laurea sperimentale

Candidato:

Flavia Aleotti

Relatore:

Prof. ssa Letizia Sambri

Correlatori:

Dott. Elia Matteucci
Dott. Michele Mancinelli
Dott. Filippo Monti

Anno Accademico 2016/2017

Contents

Abstract

Borazaro compounds (or azaborines) are aromatic compounds in which a C=C unit is replaced by an isoelectronic B−N unit. The possibility to generate chemical diversity has led to an increasing interest in azaborines, especially in the fields of biomedical research and optoelectronics. In particular, Dewar's synthesis of borazaronaphthalene is a common starting step to obtain different 1,2-azaborines via nucleophilic substitution on the boron atom.

Here we present the synthesis of a novel 1,2-azaborine (*i.e.* 4-methyl-2-(pyridin-2-yl)-2,1-borazaronaphthalene, named **FAAH**) via functionalization of 2-chloro-4-methyl-2,1-borazaronaphthalene with a 2-pyridyl unit. This compound can be used as an anionic bidentate ligand for transition metal complexes, since it can chelate the metal center with both the pyridine and the azaborine nitrogen atoms.

FAAH was used for the synthesis of a series of neutral luminescent Ir(III) complexes (named **FAV**, **FAB** and **FAR**) of general formula $[Ir(C\hat{}N)_2(\mathbf{FAA})]$, where C^N indicates three different cyclometalating ligands: *i.e.* 2-phenylpyridine in the case of **FAV**; 2-(2,4-difluorophenyl)pyridine in the case of **FAB**; 2-methyl-3-phenylquinoxaline in the case of **FAR**.

The reaction yields are quite low, however it was always possible to characterize all the compounds by means of NMR spectroscopy. A complete photophysical and theoretical characterization is also presented. **FAAH** displays a good chemical stability and high photoluminescence quantum yield (up to 28 % in solution). On the contrary, the Iridium complexes undergo degradation over time in solution. Despite this stability problem, it was possible to get a good understanding of the photophysics of the three complexes: the emission of both **FAV** and **FAB** is observed around 500 nm and arises from a ^{3}LC state centered on the azaborine ligand. In the case of **FAR**, the emitting state is probably ^{3}MLCT/^{3}LLCT in nature and the resulting broad and unstructured emission band is centered around 700 nm.

Chapter 1

Introduction

1.1 Azaborines

The introduction of heteroatoms in organic compounds is a very popular strategy to generate chemical diversity. The replacement of a C=C with an isoelectronic B−N unit in aromatic systems leads to borazaro compounds (also called azaborines), a class of compounds that has generated much interest in the last few years, especially in the fields of biomedical research and optoelectronic materials [1].

The first example of C=C/B−N substitution was reported by Alfred Stock in 1926 with the synthesis of borazine (c−$B_3N_3H_6$), the inorganic counterpart of benzene [1, 2]. Since this pioneering work, the isoelectronic relationship between B−N and C=C has led to the development of aromatic systems only partially substituted with boron and nitrogen.

The replacement of one aromatic sp^2 C=C unit with an isoelectronic B−N in benzene, generates three possible isomers, referred to as 1,2-azaborine, 1,3-azaborine and 1,4-azaborine, with different physical and chemical properties (Figure 1.1) [1].

Among these, 1,2-azaborines have been much investigated, due to the simple and robust method for their synthesis. Both theoretical calculations and experimental data have proven that the aromaticity and thermal stability of 1,2-azaborines are only slightly lower than those of the corresponding C=C aromatic systems [3].

Despite the fact that they have the same number of valence electrons and a similar stability, there are some differences between 1,2-azaborines and the corresponding "all carbon" analogues, which arise from the fact that N−B bond is polarized. This local dipole moment can significantly alter the character of the frontier molecular orbitals and the intermolecular interactions in the solid phase [4].

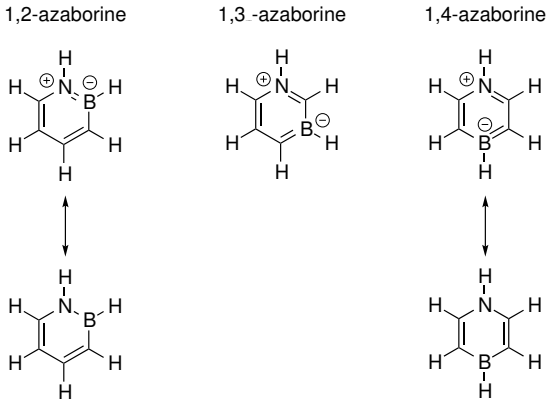

Figure 1.1: Isomeric forms of singly substituted aromatic CBN heterocycles.

There are two main fields of application of 1,2-azaborines:

1. pharmaceutical and agrochemical applications, where they have attracted much attention for the possibility to increase structural diversity [3];
2. material science, since 1,2-azaborines show interesting photophysical properties [5].

The interaction between the π orbitals and the donor/acceptor orbitals of nitrogen and boron respectively can substantially decrease the HOMO-LUMO gap, while an efficient π-conjugation is ensured by molecular planarity [6]: both of these characteristics make most azaborines luminescent, allowing for application in light emitting diodes (OLEDs) [3].

The first singly B−N substituted aromatic compounds were synthesized by Dewar in 1958: he reported the synthesis of BN-phenantrene derivatives via 9,10-azaborophenantrene **II** (see Scheme 1.1 on the facing page) [7, 8].

One year later Dewar and Diez were able to synthesize the first 2,1-borazaronaphthalene **III** by reacting 2-aminostyrene with BCl_3 [9]. Besides, it is possible to functionalize compound **III** on boron via nucleophilic substitution using different nucleophiles such as Grignard reagents (see Scheme 1.2 on the next page).

Afterwards, the discovery of many different methods to functionalize the 2,1-borazaronaphthalene core has opened the way for the synthesis of many different structures and has therefore extended the potential for additional applications [10]. Among these functionalization methods, one of the most recent and interesting is that developed by Molander et al. [3] (see Scheme 1.3). This method allows for the direct synthesis of functionalized 2,1-borazaronaphthalenes (**IX**) under mild reaction conditions via Lewis acid promoted annulation/aromatization of substituted 2-aminostyrenes **VII** with potassium organotrifluoroborates **VIII**.

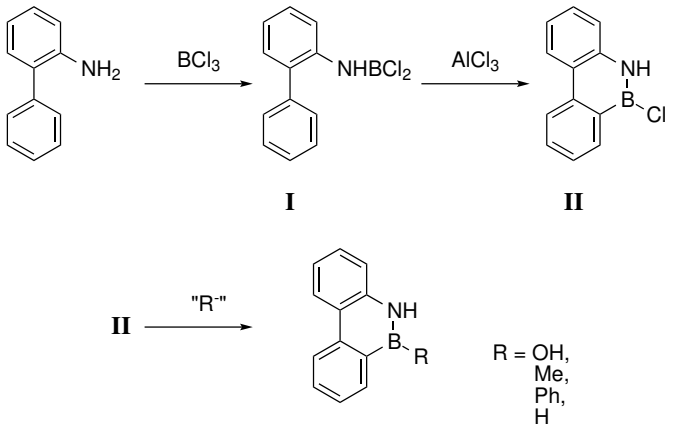

Scheme 1.1: Dewar's synthesis of boron-substituted 9,10-azaboraphenantrene derivatives.

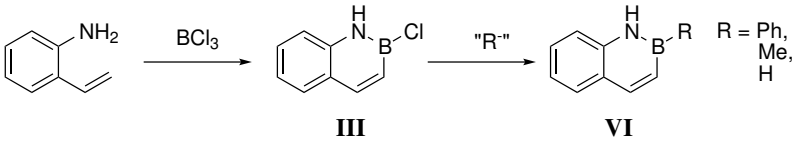

Scheme 1.2: Synthesis and functionalization of 2,1-borazaronaphthalene **III**.

Starting from 2,1-borazaronaphthalene via appropriate functionalization on the boron atom (e.g. pyridine) it is possible to construct a library of novel bidentate ligands for transition metal complexes. Luminescent complexes containing 1,2-azaborines as ligands could be conveniently used for optoelectronic applications such as in OLEDs [11].

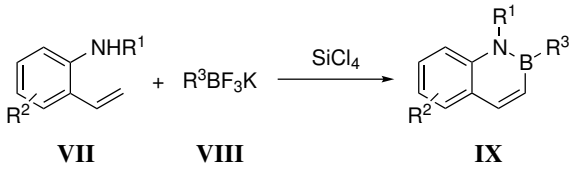

Scheme 1.3: Direct synthesis of 1,2-azaborines via R^3BF_3K

1.2 Iridium complexes for optoelectronic applications

Luminescent Transition Metal Complexes (TMCs) have been widely investigated for application in optoelectronic devices such as OLEDs and LECs because of their tunable optical properties, together with facile synthesis [12]. In addition, they are typically highly phosphorescent emitters, which allows for greater electroluminescence efficiencies compared to singlet emitters [13].

Among all TMCs, the class of Ir(III) complexes has proven to be the most versatile thanks to a unique combination of physical and chemical properties: cyclometalated Ir(III) complexes exhibit bright and tunable phosphorescent emission covering the whole visible spectrum from blue to red, together with high photoluminescence quantum yields and good chemical stability.

1.2.1 Structural properties

The typical coordination compounds of Ir(III) are octahedral complexes, which can be classified into two main families, according to the nature of the ligands:

- **homoleptic complexes**, containing three identical cyclometalated ligands;
- **heteroleptic complexes**, containing two cyclometalated ligands and one so-called "ancillary" ligand.

As selected examples for these two classes of complexes, $Ir(ppy)_3$ and $[Ir(ppy)_2bpy]^+$ are reported in Figure 1.2.

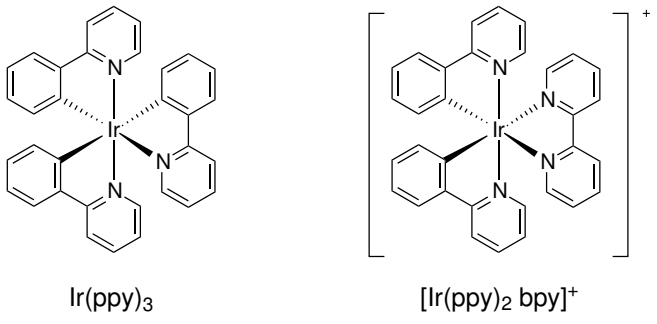

Figure 1.2: Structures of the archetypal complexes for homoleptic ($Ir(ppy)_3$) and heteroleptic ($[Ir(ppy)_2bpy)]^+$) Iridium(III) complexes

Homoleptic complexes are usually prepared either by treating $Ir(acac)_3$ (acac = acetylacetonate) with excess of the desired cyclometalating ligand, or by the reaction of $IrCl_3 \cdot nH_2O$ with a Silver(I) salt using the cyclometalating ligand as

a solvent [14, 15]. Both of the latter synthetic procedures require high temperatures (>180 °C) but many potential cyclometalating ligands are intolerant to these conditions. A two-step synthesis that requires lower temperature was described by Nonoyama in 1974 [16]: $IrCl_3 \cdot nH_2O$ is reacted with an excess of a cyclometalating ligand using refluxing 2-ethoxyethanol as solvent (bp: 130 °C). The product of this reaction is a μ-dichloro-bridged dimeric complex with formula $[Ir(C\text{^}N)_2Cl]_2$, with the heterocyclic rings of the (C^N) ligands in a *trans* disposition [17] (Scheme 1.4).

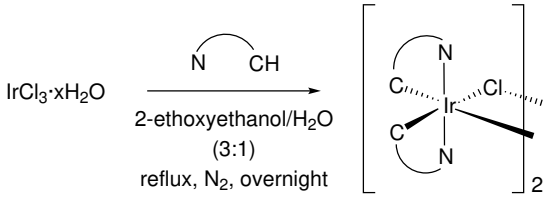

Scheme 1.4: General procedure for the synthesis of Ir(III) dimers.

These Ir(III)-dimers can serve as precursors for tris-cyclometalated complexes by several routes, but they also serve as intermediates in the general procedure for the synthesis of heteroleptic complexes when treated with an appropriate ancillary ligand. Actually, there are three different families of ancillary ligands that can be used: monoanionic, dianionc and neutral, which are chosen to obtain neutral, anionic or cationic complexes, respectively. Monoanionic ligands are the most suitable for OLED application, since they allow the device preparation via vacuum sublimation of the neutral emitter, while ionic complexes are more suitable for LECs, which require charged active materials. To promote the formation of the final complexes, a silver ion can be used to remove the bridging chlorides in the presence of the desired ligand [18].

Tris-cyclometalated Ir(III) complexes can present two different geometries: *facial* (*fac*-) or *meridional* (*mer*-) isomers (Figure 1.3 on the following page, **a** and **b**). All the reported synthetic methods typically lead to the formation of the *fac*-isomer as the major product. The reason for this outcome is related to the so called "*trans* effect" of the Ir−C bonds: these induce preferential labilization of the bonds located *trans* to them, which results in the stereochemical positioning of Ir−C and Ir−N *trans* to one another [17].

Unlike tris-cyclometalated complexes, the geometry for Ir-dimers is "*mer*-like" (see Figure 1.3, **c**). When using a dichloro-bridged complex as a precursor, either the *fac*- or the *mer*-isomer of the final complex can be obtained, depending on the reaction conditions: if the reaction is performed at high temperature (180 °C) the final isolated complex is the thermodynamically more stable *fac*-isomer, while

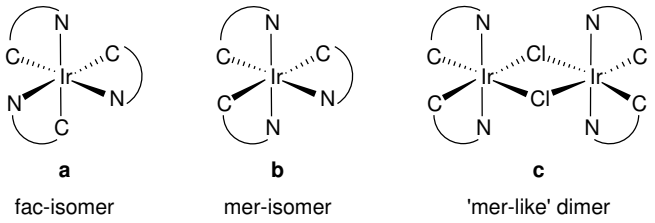

Figure 1.3: Geometry of tris-cyclometalated Ir(III) complexes (**a**, **b**) and dimeric form (**c**).

if the temperature is kept lower (<150 °C) it is possible to obtain the *mer*-isomer as the only product. The *mer*-isomer can be subsequently converted, either thermally or photochemically, into the more stable *fac*-isomer.

1.2.2 Electronic properties

The d orbitals of the metal center in a general TMC are destabilized and split in an octahedral ligand field into two sets: t_{2g} orbitals (d_{xy}, d_{xz}, d_{yz}) lie lower in energy, while e_g orbitals (d_{z^2}, $d_{x^2-y^2}$) lie at higher energy (Figure 1.4 on the next page). The energy difference between these two sets of orbitals (Δ_o) depends on:

1. the oxidation state of the metal center (the higher oxidation state, the higher the Δ_o);
2. the spatial extension of the d orbitals (Δ_o increases progressively going from 3d to 4d and 5d metals);
3. the field strength exerted by the ligands (*i.e.* spectrochemical series).

The Δ_o in the case of Ir(III) complexes is high due to (i) the highly charged metal ion, (ii) the presence of 5d orbitals, and (iii) the strong-field ligands (*i.e.* anionic cyclometalating ligands). As a result, the metal center always shows a low-spin electronic configuration ($t_{2g}^6 e_g^0$) and the ligand-field stabilization energy is maximized.

Since the electronic configuration of the Ir(III) ion is $5d^6$, the related organometallic compounds have a closed-shell electronic configuration. As a consequence, the ground state of the complexes is a singlet (S_0 - see Figure 1.4 on the facing page).

Light absorption in all transition metal complexes can promote spin-allowed electronic transitions from the ground state (GS, which is S_0 in the case of Iridium(III)) to other electronic states with the same spin multiplicity of various nature and electronic localization [17]. In the case of Ir(III) complexes, this can result

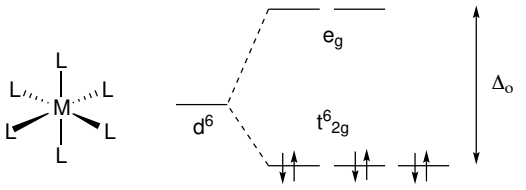

Figure 1.4: Low-spin d^6 electronic configuration in octahedral field

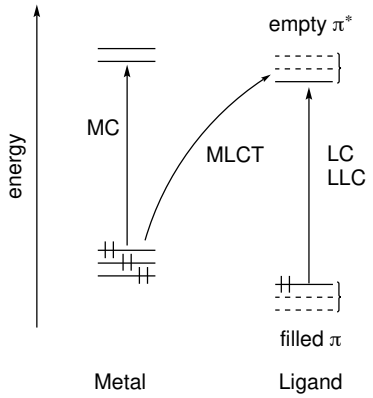

Figure 1.5: Orbital description of MC, LC, MLCT and LLCT transitions in Ir(III) complexes

in ligand-centered (^{1}LC), metal-centered (^{1}MC), metal-to-ligand charge transfer (^{1}MLCT) and ligand-to-ligand charge transfer (^{1}LLCT) transitions, as depicted in Figure 1.5.

Moreover, for complexes with a heavy-metal center (as Iridium), intersystem crossing efficiency from and to states of different spin multiplicity is almost unitary, due to the "heavy atom effect" which causes a high spin-orbit coupling. As a result, in Ir(III) complexes, singlet to triplet intersystem crossing is almost unitary, and emission always arises from triplet levels (*i.e.* phosphorescence) ^{3}MLCT or ^{3}LC in nature, which actually include changeable amounts of the corresponding singlets [17].

Depending on the contribution of the charge transfer (CT) states, the emission profile is substantially affected: the presence of vibrational features suggests a low CT character, whereas a broad and unstructured shape indicates a high charge transfer character. Rigidochromic effect could also be used to assess the CT nature of the emission: CT levels usually undergo blue shift on passing from fluid to solid polar solvent, while ^{3}LC levels are substantially unaffected under the same conditions [17]. Similarly, the wavelength of the emission maximum is dependent on the polarity of the solvent in the case of a high CT character (*i.e.* solvatochromic effect).

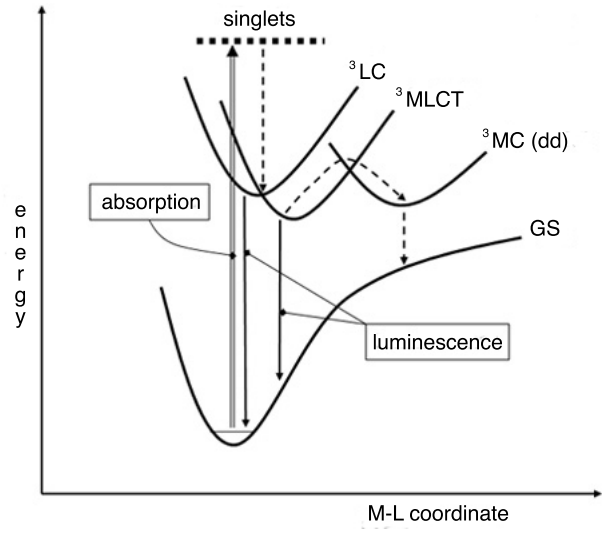

Figure 1.6: Electronic transitions involving MC, MLCT and LC excited states; the MC levels are not emissive [17]

There are other transition metal ions having the same d^6 low-spin configuration as Ir(III) in the presence of strong-field ligands (*i.e.* Os(II), Ru(II) and even Fe(II)) but none of their complexes exhibits such remarkable photophysical properties (*i.e.* tunability of emission wavelength, high photoluminescence quantum yield, good photostability) because of the nature of the excited states (see Figures 1.6 and 1.7).

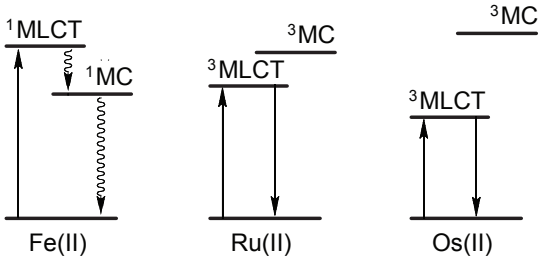

Figure 1.7: Qualitative electronic excited states description for Fe(II), Ru(II) and Os(II) metal complexes

For what concerns Fe(II) in an octahedral field, Δ_o is small and the lowest-lying excited state is most likely MC in nature and, therefore, not emissive. Ru(II) has a $4d^6$ configuration: Δ_o is increased if compared to Fe(II) and the lowest excited state in this case is a ^{3}MLCT. However, it is close enough to ^{3}MC levels that they can be thermally populated at room temperature, thus affecting the emission

intensity. Os(II) has a $5d^6$ electronic configuration and Δ_o is so high that MC levels are usually unaccessible, but the emissive ^{3}MLCT and ^{3}LC levels lie quite low in energy, favoring radiationless deactivation in accordance with the "energy gap law" [19].

Besides the just mentioned advantages of Ir(III) over other transition metal ions, the emission color tunability (from sky-blue to deep-red) of its related complexes is a crucial property for optoelectronic applications. In this context, heteroleptic Ir(III) complexes are much more versatile because of the huge number of possible combination of cyclometalating and ancillary ligands that can be prepared. Since the emission wavelength often depends on the HOMO-LUMO gap, a preliminary understanding of the molecular orbitals of the complexes is the first step to develop an effective strategy to tune their emission color.

Just to mention a relatively simple example of how an Iridium(III) complex could be molecularly engineered, we report the case of the heteroleptic cationic complex $[Ir(ppy)_2(bpy)]^+$ reported in Figure 1.2 on page 4. In this compound the HOMO is centered on the cyclometalating ligands and on the metal ion, while the LUMO is located on the ancillary ligand (Figure 1.8, left). Therefore, the lowest emitting triplet (T_1) is expected to display a mixed ^{3}MLCT/^{3}LLCT character. Actually, since a potential interplay between different triplet excited states could occur upon geometry relaxation from the Franck-Condon region, a full geometry optimization of the T_1 state should be carried out to have a final insight on the real nature of the emitting state (Figure 1.8, right).

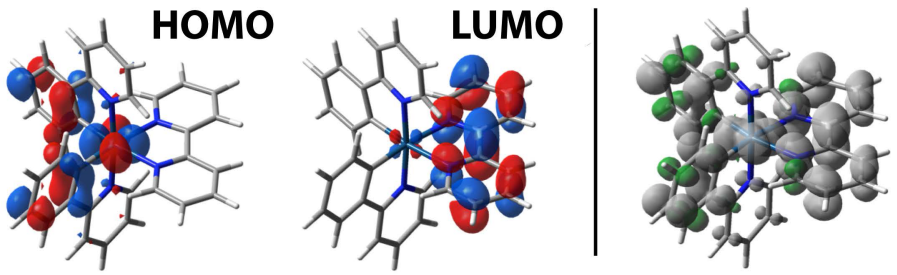

Figure 1.8: Representation of the HOMO and LUMO of $[Ir(ppy)_2(bpy)]^+$ in its optimized ground state (left) and spin-density distribution of the lowest triplet state in its minimum geometry (right).

Anyway, as a rule of thumb, since the emission wavelength could be correlated to the HOMO-LUMO gap, it is possible to plan a color-tuning strategy by stabilization/destabilization of the frontier molecular orbitals. Stabilization of the HOMO and/or destabilization of the LUMO leads to a blue shift; *vice versa*, a red-shifted emission is obtained by reducing the HOMO-LUMO gap.

Strategies to shift the emission to the blue include:

- attaching electron-withdrawing substituents (e.g. fluoride) to the cyclometalating ligands: these reduce the σ donation to the metal, thus decreasing the electron density on the Iridium ion and stabilizing the HOMO;
- using stronger field cyclometalating ligands to increase the d-d splitting;
- destabilizing the LUMO by placing electron-donating group on the ancillary ligand (e.g. amino or methoxy substituents) [12];
- replacing a "low-lying" ancillary ligand with another having higher-energy π^* orbitals.

The last two strategies, despite rather effective, have an intrinsic limit: if the LUMO of the ancillary ligand is extremely destabilized, the LUMO+1 or LUMO+2 (usually located on the cyclometalating ligands), can become the "new LUMO" of the complex, leading to an emitting T_1 with a more ligand-centered character.

Along the same line of reasoning, it is possible to obtain a red shift in the emission in several ways:

- adding electron-donating groups on the cyclometalating ligand (and particularly in *meta*-position related to the coordination site) can red-shift the emission color up to several nanometers;
- increasing the delocalization of the π system of the ancillary ligand leads to a marked bathochromic shift, the magnitude of which is dependent on the specific ligand used;
- presence of polarizable atoms: the incorporation of soft atoms, such as sulfur and nitrogen, in the cyclometalated ring system can significantly lowering the emission energies of the complexes.

For more accurate estimations, theoretical calculations performed with the time-dependent version of the density functional theory (TD-DFT) have proven to be very useful to determine the electronic nature and relative energy ordering of the low-lying triplet states. These calculations should be then followed by a full geometry optimization of the T_1 state.

As described above, the emission color of Ir(III) complexes can be readily tuned from blue to red by judicious modification of the cyclometalating ligands and/or ancillary ligands. In general, multicolor display applications require efficient and stable blue, green and red OLEDs. It is interesting to note that red and green Iridium complexes are easier to obtain and have been well developed, while it remains much more challenging to prepare blue phosphors with a high level of monochromaticity and photostability [12]. This is because wide HOMO-LUMO

gaps are more difficult to obtain and the high energy levels of blue emitters tend to be reactive under the device operating conditions. In this optic, the discover of efficient blue-emitting complexes remains a topic of a great importance for opto-electronic applications.

1.3 Purpose of the work

The aim of the present work is the synthesis and characterization of a series of phosphorescent Ir(III)-azaborine complexes with interesting photophysical properties. Appropriate functionalization on the boron atom of a 2,1-borazaronaphthalene derivative is a useful strategy to obtain a novel class of bidentate ligands to be used in transition-metal complexes. In this particular case, functionalization with a 2-pyridyl unit of 2-chloro-4-methyl-2,1-borazaronaphthalene (Figure 1.9 **a**) leads to the formation of 4-methyl-2-(pyridin-2-yl)-2,1-borazaronaphthalene (Figure 1.9 **b**, from here on named **FAAH**) that can conveniently coordinate an Ir(III) metal center through the two nitrogen atoms forming the typical five-membered ring structure (Figure 1.9 **c**).

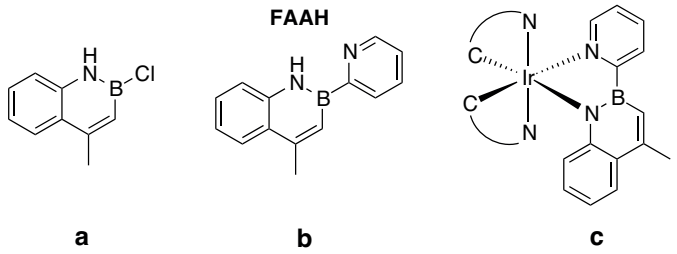

Figure 1.9: (**a**) 2-chloro-4-methyl-2,1-borazaronaphthalene; (**b**) 4-methyl-2-(pyridin-2-yl)-2,1-borazaronaphthalene (**FAAH**); (**c**) coordination of the Ir(III) metal center through nitrogen atoms

The different cyclometalating ligands were chosen in order to obtain a possible color tuning compared to the archetypal phenylpyridine complex. 2-(2,4-difluorophenyl)pyridine was used to shift the emission to the blue, while, to obtain a red-shift, we used 2-methyl-3-phenylquinoxaline. The final complexes (compounds **15**, **16** and **17**, from here on named **FAV**, **FAB** and **FAR**, respectively) are represented in Figure 1.10 on the following page.

The use of 1,2-azaborines as ligands for Ir(III) complexes could bring about new interesting properties: the substitution of an sp^2 C=C with an isoelectronic B−N, makes 1,2-azaborines aromatic, so the binding via the nitrogen atom is similar to a cyclometalation reaction, and the anionic ligand is therefore expected to be a strong field ligand. This could significantly alter the relative energy of the frontier molecular orbitals of the octahedral complexes, lending them some novel

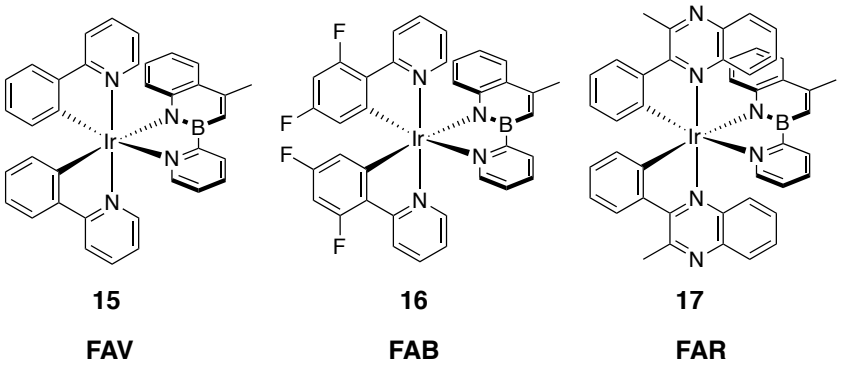

Figure 1.10: Structure of the three Ir(III)-azaborine complexes to be synthesized

properties.

1,2-azaborines display interesting photophysical properties for optoelectronic applications, nevertheless to our knowledge there are no examples in literature of Ir(III) complexes similar to the ones we report here.

Chapter 2

Results and Discussion

2.1 Synthesis of the 2,1-Borazaronaphthalene ligand

The synthesis of the azaborine ligand **FAAH** (compound **5**) was carried out using three different routes (from here on named route **A**, **B** and **C**) all of which start from the commercially available 2-isopropenylaniline (**1**).

Scheme 2.1 summarizes the three synthetic strategies.

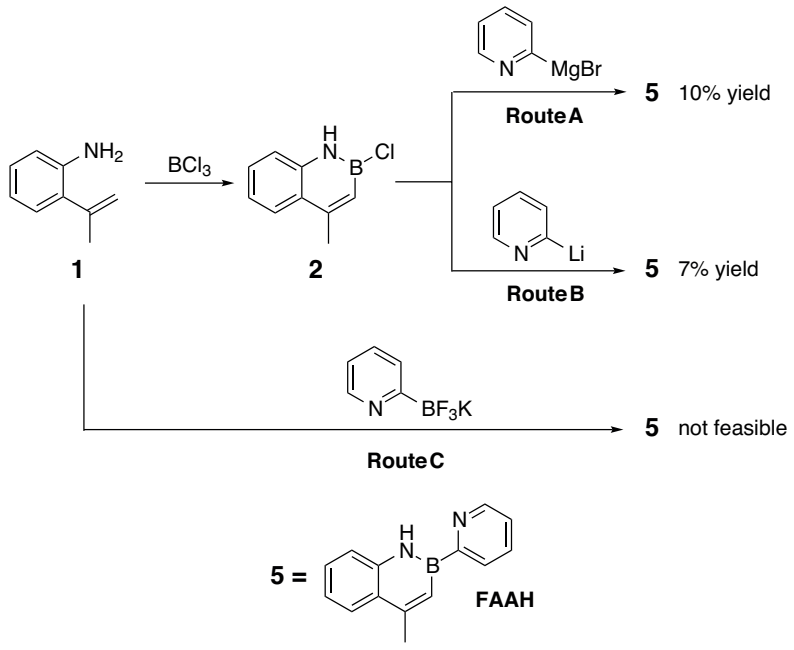

Scheme 2.1: Synthetic routes for azaborine **5** (**FAAH**)

For routes **A** and **B** the first step is the reaction of the compound **1** with BCl_3 that leads to a direct cyclization to generate intermediate **2** (Scheme 2.2) [7].

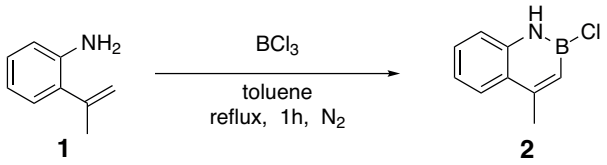

Scheme 2.2: Synthetic procedure for intermediate **2**

Aniline **1** was dissolved in toluene under nitrogen atmosphere at 0 °C, then a 1 M solution of BCl_3 was added dropwise. The solution was refluxed for 1 hour, then the excess BCl_3 was stripped using a vacuum pump after cooling to room temperature.

Once the intermediate **2** is formed, it can undergo nucleophilic substitution at the reactive B-Cl unit.

For route **A** a Grignard reagent (**4**) was used as a nucleophile. It was prepared *in situ* from 2-Bromopyridine (**3**) as represented in Scheme 2.3.

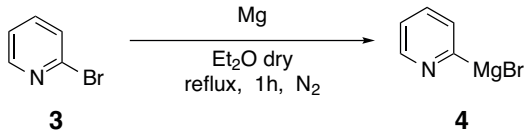

Scheme 2.3: Synthetic procedure for Grignard reagent **4**

The Mg was first activated using a diluted HCl water solution (0.1 M), then it was stirred in dry Et_2O under nitrogen atmosphere overnight. 2-Bromopyridine was then added dropwise together with a catalytic amount of iodoethane. The solution was refluxed for 1 hour, after which the Grignard reagent **4** was added dropwise to the solution containing intermediate **2** as reported in Scheme 2.4 on the next page. The solvent was then removed in vacuum and the resulting crude was purified on silica gel. Product **5** (**FAAH**) was obtained with a 10% yield.
The ^{1}H NMR spectrum of the azaborine product **5** (in $CDCl_3$ at 600 MHz, see the experimental section) shows some peculiar signals like the $-$NH large singlet at 9.38 ppm, and the $-CH_3$ doublet at 2.70 ppm.

In route **B** 2-Lithiumpyridine (**6**) was used as a nucleophile. Like the Grignard reagent, it was prepared *in situ* via reaction of 2-Bromopyridine (**3**) with *n*-Butyllithium, as represented in Scheme 2.5 on the facing page.

Reagent **3** was dissolved in THF under nitrogen atmosphere. The solution was then cooled up to −78 °C. *n*-Butyllithium was then added dropwise to get an orange solution containing product **6**.

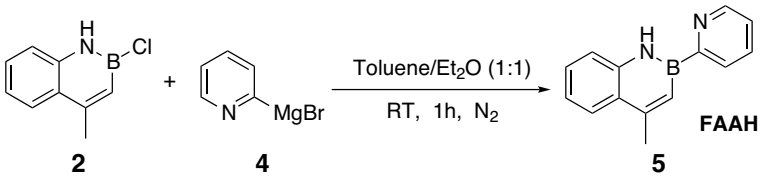

Scheme 2.4: Synthetic procedure for the azaborine ligand **5** via Grignard reagent

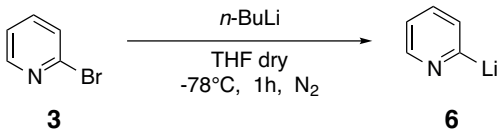

Scheme 2.5: Synthetic procedure for 2-Lithiumpyridine **6**

The B-Cl intermediate **2** was prepared in the same way as before (see Scheme 2.2 on the preceding page). Once the intermediate **2** was formed, the solution of 2-Lithiumpyridine **6** was added dropwise at −78 °C, then the mixture was left to reach room temperature and stirred overnight. The solvent was then removed in vacuum and the resulting crude was purified on silica gel. The ^{1}H NMR spectrum of the obtained product **5** (**FAAH**) recorded in $CDCl_3$ showed the peculiar signals listed before.
The yield for **FAAH** via route **B** was 7%.

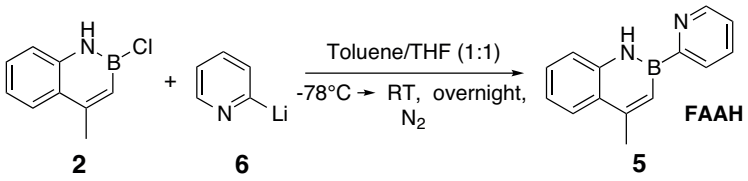

Scheme 2.6: Synthetic procedure for the azaborine product **5** via 2-Lithiumpyridine **6**

The yield of routes **A** and **B** was low mainly because of the instability of the pyridine carbanion and because of the reactivity of the B-Cl intermediate. This leads to the formation of several side products like **7a** and **7b** (see Figure 2.1). These are formed by the reaction of **2** with the OH^- nucleophile, which is inevitably present [20].

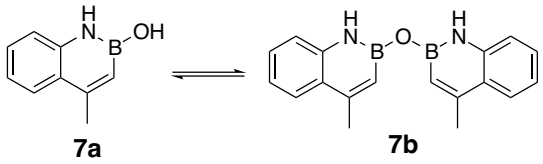

Figure 2.1: Stucture of the main side products **7a** and **7b**

To reduce the probability of having side products, we tried to synthesize the azaborine **FAAH** via route **C**. The idea is to treat the starting aniline **1** with potassium pyridine-2-trifluoroborate (**8**) to get **FAAH** directly (Scheme 2.7), following a reported method for the synthesis of *B*-heteroaryl-substituted 2,1-Borazaronaphthalenes [10].

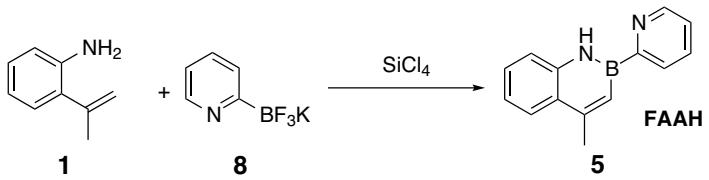

Scheme 2.7: Synthetic procedure for azaborine **5** via route **C**

The first step is the synthesis of the $-BF_3K$ derivative. 2-Lithiumpyridine **6** used in route **B** was prepared *in situ* in the same way (see Scheme 2.5 on the preceding page). Product **6** was then treated with $B(OMe)_3$ and a KHF_2 water solution to get the potassium pyridine-2-trifluoroborate **8** [21]. The mixture was vigorously stirred overnight to avoid phase separation. Scheme 2.8 reports the reaction conditions.

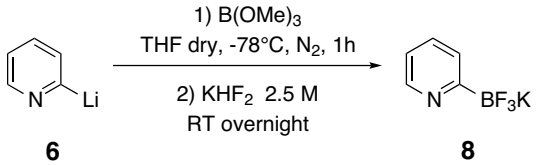

Scheme 2.8: Synthetic procedure for product **8**

The organic phase was then separated, the solvent was removed in vacuum and the crude was purified on silica gel. The product potassium pyridine-2-trifluoroborate (**8**) was obtained with a 5% yield.

Product **8** was identified via both ^{1}H NMR and ^{19}F-NMR spectra. In particular, the ^{19}F-NMR spectrum showed only one signal, which was the quartet of the $-BF_3K$ at -147.4 ppm, due to the coupling between ^{19}F (spin 1/2) and ^{11}B (spin 3/2).

Because the yield was so low even in the first step, it was not convenient to move on to the next step of the synthesis, and ligand **FAAH** was eventually prepared as described in routes **A** and **B**.

2.2 Synthesis of Ir(III) dimers

The cyclometalating ligands used for the synthesis of the RGB series of Iridium complexes are represented in Figure 2.2.

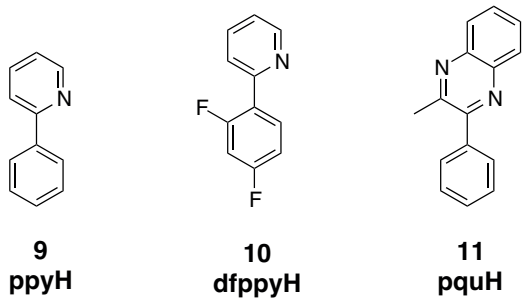

Figure 2.2: Structure of the cyclometalating ligands **9**, **10** and **11**

Ligand **9** is used as a reference since the 2-Phenylpyridine Iridium complexes are very popular an well known [22]. The other two ligands were chosen because of their ability to shift the emission to the blue (ligand **10**) or to the red (ligand **11**) compared to the Ir(III)−ppy complexes [23].

Ligands **9** and **10** are commercially available, while 2-methyl-3-phenylquinoxaline (**11**) was synthesized through the double condensation of 1,2-diaminobenzene and 1-phenyl-1,2-propanedione in presence of I_2 as catalyst, following a described procedure [24].

The synthesis of the Ir(III) dimers was carried out following the general procedure reported by Nonoyama in 1974 [16]. $IrCl_3{\cdot}nH_2O$ was reacted with 2 equivalents of cyclometalating ligand to obtain the corresponding dimer, as reported in Scheme 2.9 on the next page. In Iridium dimer complexes, the two Ir−C bonds are stereochemically cis to each other, whereas the Ir−N are mutually in *trans* position.

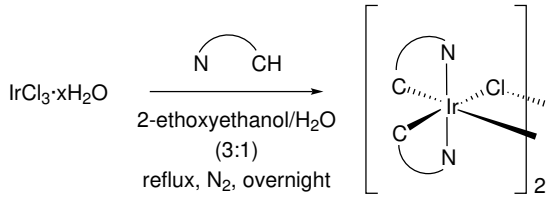

Scheme 2.9: General procedure for the synthesis of Ir(III) dimers

The cyclometalation reaction is a two-step process that consists in the binding of the donor group of the aromatic heterocycle to the metal centre, followed by intra-molecular cleavage of the C–H bond, forming the metal-containing cyclic framework [25, 26]. The reaction requires high temperatures, therefore all reagents were dissolved in a 3:1 mixture of 2-ethoxyethanol and water and refluxed overnight under N_2 atmosphere. As the dimer is formed, it precipitates as an insoluble solid. The precipitation was eventually completed by adding more water, then the obtained solid was filtered and washed with H_2O and hexane.

The structures of the obtained dimers are reported in Figure 2.3.

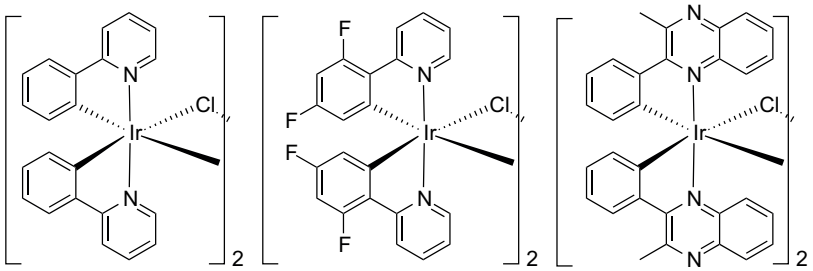

Figure 2.3: Structure of Ir(III) dimers **12**, **13** and **14**

The ^{1}H NMR spectra of the dimers **12** and **13** are in accordance with those found in literature [27, 28]. A full characterization of complex **14** is not available in literature, nevertheless the signals in its ^{1}H NMR spectrum (in $CDCl_3$ at 400 MHz, see the experimental section) were congruent with the expected product.

2.3 Synthesis of the Ir(III)-2,1-Borazaronaphthalene complexes

The screening of the reaction conditions to obtain the desired Ir(III)-azaborine complexes was performed using compound **12** as Ir(III) precursor.

Some considerations about the azaborine **FAAH** can help to design an effective synthetic strategy. The B−N unit is isoelectronic with a C−C bond. This CC/BN isosterism makes the 1,2-azaborine ring aromatic, and the whole compound **5** (**FAAH**) is therefore similar to a third cyclometalating ligand.
This means that the −NH hydrogen is quite difficult to remove, even because it is involved in a strong hydrogen bond with the nitrogen of the pyridine moiety. That's why the first attempts to bind **FAAH** to the Ir(III)-ppy dimer were carried out under severe conditions (*i.e.* high temperature in the presence of a base to encourage deprotonation; the deptoronated **FAAH** in the Ir(III) complexes will be named **FAA**). Scheme 2.10 represents the general screening reaction, while Table 2.1 summarizes the reaction conditions used in the different attempts.

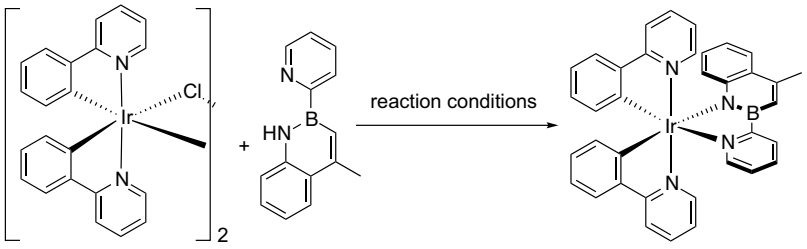

Scheme 2.10: General reaction scheme for the synthesis of complex **15** (**FAV**)

Table 2.1: Screening of the reaction conditions for the synthesis of complex **15** (**FAV**)

Entry	Solvent	Base	Temperature °C	Additive	Yield (%)
A	2-ethoxyethanol/H_2O (3:1)	-	≃+130 (reflux)	-	-
B	2-ethoxyethanol	K_2CO_3	+135.6 (reflux)	-	-
C	DCM/EtOH (3:1)	K_2CO_3	RT	-	-
D	DCM/EtOH (3:1)	KOH	RT	$AgBF_4$ (dark)	-
E	DCM/EtOH (3:1)	-	RT	$AgBF_4$ (dark)	8
F	DCM/EtOH (3:1)	NaH	RT	$AgBF_4$ (dark), ACN/Et_2O	32

Entry A In a first synthetic strategy, we tried to bind ligand **FAAH** (**5**) via classical cyclometalation reaction (without adding any base). Unfortunately, this synthetic approach did not bring any interesting results; the ^{1}H NMR spectrum of the

crude was full of aromatic signals, none of which could however be ascribed to the expected complex **FAV** (**15**).

Entry B In a second strategy we tried add a base (K_2CO_3), following a general procedure for tris-cyclometalated Ir(III) complexes reported in literature [29]. The solvent was degassed by bubbling N_2, then the azaborine ligand **5** was added together with K_2CO_3 and the solution was stirred at room temperature for 15 minutes. The dimeric ppy-Ir(III) complex was eventually added and the reaction was refluxed overnight.

The ^{1}H NMR spectrum of the resulting crude showed a lot of aromatic signals, which however were not in accordance with those expected for complex **15** (**FAV**) but were not even ascribable to the starting products. The boiling temperature of the solvent (135.6 °C) was probably too high and may have caused the degradation of the azaborine ligand.

Entry C The third synthetic attempt was performed at room temperature, using a 3:1 mixture of DCM/EtOH as a solvent. The base K_2CO_3 was kept unchanged. The dimeric ppy-Ir(III) complex was added to a solution of **FAAH** (**5**) and K_2CO_3. The mixture was then stirred overnight at room temperature.

Again the ^{1}H NMR spectra of the crude and purified fractions did not show any interesting signals, probably due to the binding of Ir(III) just to the nitrogen of the pyridine moiety (no deprotonation) or to the formation of side-products.

Entry D In a fourth synthetic strategy, we have tried to make reagent **12** more reactive by removing the chlorides from the dichloro-bridged dimer by treating with $AgBF_4$ [18, 23].

The azaborine ligand **FAAH** (**5**) was pre-treated with a stronger base (KOH was used instead of K_2CO_3) in accordance with a reported method [30].

Ir(III) dimer **12** was dissolved in DCM, then $AgBF_4$ was added in the absence of light and the mixture was stirred at room temperature. After 24 hours the yellow solution obtained by the activation of **12** was separated from the dark precipitate and an ethanol solution of **FAAH** (**5**) and KOH was added. As soon as the two solutions were mixed together, the mixture became dark. The crude was eventually purified on Al_2O_3, to obtain a yellow-green luminescent product.

The ^{1}H NMR spectrum of the collected fractions showed some signals that could fit those of the expected complex: the signals of the cyclometalating ligand **9** were doubled because of the loss of symmetry, while the signals of the azaborine **FAAH** were a bit shifted. Even if it was possible to identify the desired product, the result was not so good as the signals were quite weak and the spectrum showed a lot of other signals, including those of the starting dimeric complex (**12**) and of the free ligand (**5**).

It was not possible to determine the reaction yield as the collected amounts were so little and the product showed not to be pure but a mixture of starting materials, desired product and maybe also byproducts.

Entry E We tried to perform the same reaction as in the previous synthetic strategy (see Entry **D**) but in the absence of KOH, to verify if the presence of the base was really necessary or if something different could happen.

After 24 hours, the ^{1}H NMR of the crude only showed the signals of the starting materials **12** and **5**. Some more $AgBF_4$ was then added to make the dimeric complex even more reactive, and after a few minutes the solution became dark. The mixture was purified on basic Al_2O_3. Complex **FAV** (**15**) was obtained with a 8% yield.

Entry F The activation of the dimeric Ir(III) complex showed to be a good method, but the whole synthetic procedure still had some problems and the final yield was quite low. When adding extra $AgBF_4$, we observed not only the precipitation of AgCl, but also the formation of a dark soluble product which lowered the yield, even if it was not possible to isolate and identify it. To avoid this, the activated Ir(III) dimer was precipitated as a solvato-complex (**S1**) using acetonitrile, following a reported method [18, 31].

In addition, the fact that it was possible to synthetise the final complex even without pre-treating the azaborine ligand with KOH means that the base was not efficiently deprotonating ligand **FAAH** , so we needed to use a stronger one if we wanted to remove the −NH hydrogen and make the azaborine more reactive.

After treating the Ir(III) dimer **12** with $AgBF_4$, the solution was filtered on a PTFE filter to remove the AgCl precipitate and the activated Ir(III) complex was transformed into a solvato-complex (**S1**) using acetonitrile. **S1** was then precipitated by adding Et_2O and dried under vacuum.

At the same time, **FAAH** (**5**) was dissolved in DCM and pre-treated with NaH. The ligand and the base were stirred together for a few hours before the addition to a DCM solution of **S1**. Scheme 2.11 on the next page resumes the reaction procedure for Entry **F**.

The resulting yellow crude was purified on basic Al_2O_3 to give product **FAV** (**15**) with a 32% yield.

This last approach showed to be much better than the previous one, and the yield was significantly increased. The same synthetic procedure was then applied for the synthesis of complexes **FAB** (**16**) and **FAR** (**17**) that were obtained with 25% and 11% yield respectively.

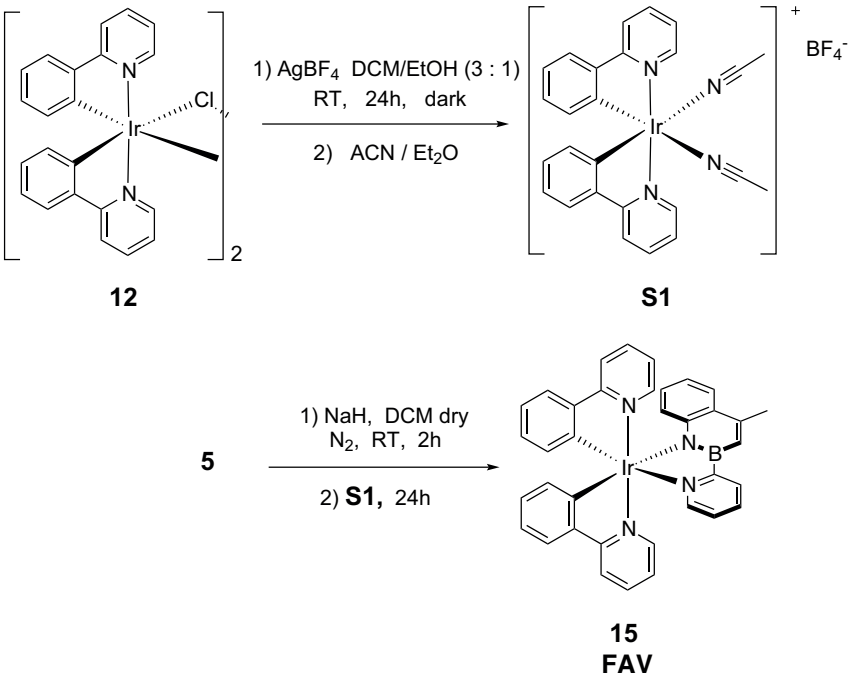

Scheme 2.11: Synthesis of complex **FAV** (compound **15**) via solvato complex **S1**

2.4 Photophysical characterization

2.4.1 2,1-Borazaronaphthalene ligand

The photophysical characterization of the ligand **FAAH** was performed both in acetonitrile (ACN) and in dichloromethane (DCM) solution. Since **FAAH** has a basic site on the pyridine moiety, it was also possible to obtain and characterize its protonated form $\mathbf{FAAH_2^+}$ by adding a stoichiometric amount of trifluoroacetic acid to the **FAAH** solution (*vide infra*). The singlet ground state (S_0), the first excited singlet (S_1) and the lowest triplet (T_1) were optimized by means of theoretical calculations as described in the computational details.

The absorption spectra of **FAAH** and $\mathbf{FAAH_2^+}$ in dichloromethane and acetonitrile recorded at room temperature are reported in Figure 2.4 and the relative absorption maxima are reported in Table 2.2 on the next page.

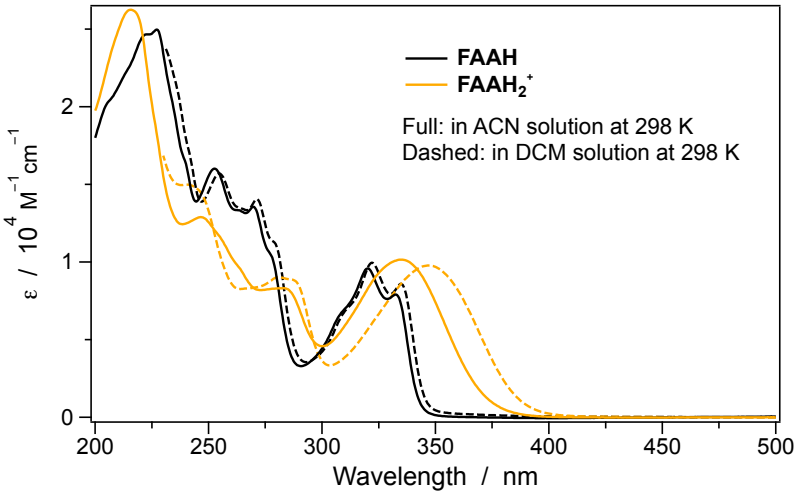

Figure 2.4: Absorption spectra of **FAAH** and $\mathbf{FAAH_2^+}$ in room-temperature dichloromethane (DCM) and acetonitrile (ACN) solutions

The absorption spectrum of **FAAH** is almost solvent independent and only a minor blue shift is observed passing from dichloromethane to the more polar acetonitrile (appox. 3 nm).

On the contrary, the spectrum of $\mathbf{FAAH_2^+}$ is more broadened and unstructured and the absorption maximum around 350 nm is significantly blue shifted passing from dichloromethane to the more polar acetonitrile solution: these features are ascribable to a charge-transfer (CT) transition from the borazaronaphthalene unit to the protonated pyridine moiety.

The absorption spectrum of a 40 μM solution of **FAAH** was also recorded upon

Table 2.2: Absorption maxima of **FAAH** and its protonated form $\mathbf{FAAH_2^+}$ in solution at 298 K (sh = shoulder)

	Acetonitrile		Dichloromethane	
	λ_{max} (nm)	ϵ ($\cdot 10^4$ $M^{-1}cm^{-1}$)	λ_{max} (nm)	ϵ ($\cdot 10^4$ $M^{-1}cm^{-1}$)
FAAH	333	0.80	335	0.86
	320	0.96	322	1.00
	309 (sh)	0.68	309 (sh)	0.65
	277 (sh)	1.06	280 (sh)	1.10
	269	1.36	272	1.41
	253	1.60	255	1.57
	227	2.50		
$\mathbf{FAAH_2^+}$	335	1.02	347	0.98
	283	0.83	281	0.90
	247	1.29	240	1.5
	215	2.63		

addition of increasing amounts of trifluoroacetic acid in dichloromethane (up to 500 equivalents, see Figure 2.5). In this range several isosbestic points are found, attesting to the occurrence of one single reaction (*i.e.* the protonation of **FAAH** at the pyridine nitrogen).

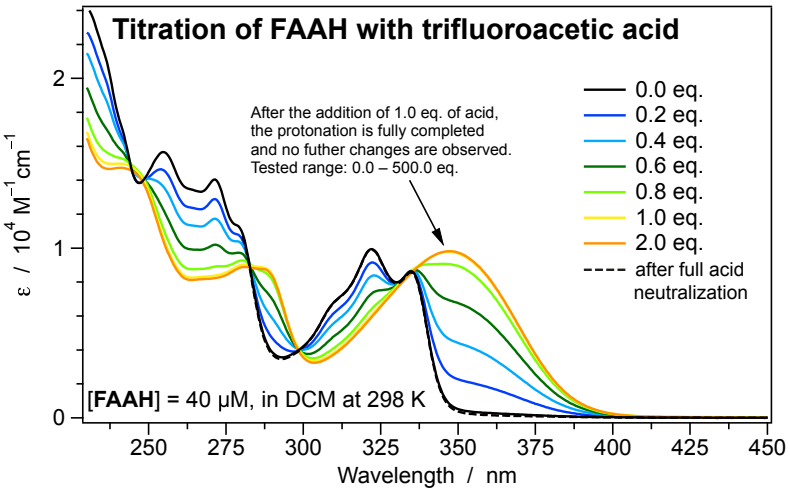

Figure 2.5: Absorption spectral changes of **FAAH** upon addition of increasing amounts of trifluoroacetic acid in room-temperature dichloromethane, range between 0 and 2 equivalents.

Thanks to TD-DFT calculations, the observed absorption bands can be attributed to specific electronic transitions. Table 2.3 on the next page summarizes

Table 2.3: TD-DFT Singlet excited states calculated for **FAAH** and $\mathbf{FAAH_2^+}$ in acetonitrile. Vertical excitation wavelength (λ), oscillator strength (f), dominant monoexcitations (with their contribution in parentheses) and nature of the electronic transition are provided (napht = borazaronaphthalene, py = pyridine).

state	λ (nm)	f	dominant monoexcitation	nature
			FAAH	
S_1	311	0.616	HOMO⟶LUMO (94%)	napht/py⟶napht and py
S_2	283	0.003	HOMO-2⟶LUMO (84%)	py⟶napht and py
S_3	282	0.068	HOMO-1⟶LUMO (88%)	napht⟶napht and py
S_4	261	0.463	HOMO⟶LUMO+1 (73%)	napht/py⟶napht and py
S_5	247	0.062	HOMO⟶LUMO+2 (73%)	napht/py⟶py
			$\mathbf{FAAH_2^+}$	
S_1	363	0.452	HOMO⟶LUMO (89%)	napht⟶py
S_2	342	0.020	HOMO-1⟶LUMO (87%)	napht⟶py
S_3	296	0.124	HOMO⟶LUMO+1 (89%)	napht⟶py
S_4	281	0.134	HOMO-1⟶LUMO+1 (90%)	napht⟶py
S_5	263	0.212	HOMO⟶LUMO+2 (82%)	napht⟶napht and py

the vertical excitation energies and electronic nature of the transitions calculated for both **FAAH** and $\mathbf{FAAH_2^+}$ in their respective singlet ground state minimum conformation.

In order to allow an easy attribution of the nature of the transitions, the frontier molecular orbitals are reported in Figure 2.6 on the following page, together with their associated energies.

For both **FAAH** and $\mathbf{FAAH_2^+}$ the population of the S_1 state from S_0 is associated with a HOMO⟶LUMO transition with a high oscillator strength. In the neutral molecule, the HOMO and the LUMO are rather distributed throughout the whole molecule, even if the latter displays a grater contribution from the pyridine orbitals. As a consequence the LUMO is more stabilized than the HOMO by the protonation on the pyridine moiety, leading to a reduction of the HOMO-LUMO energy gap in the case of $\mathbf{FAAH_2^+}$.

The topology of the frontier molecular orbitals is similar in the two species, but in the protonated form the HOMO is almost completely localized on the borazaronaphthalene moiety, while the LUMO is totally localized on the pyridine moiety. This confirms the experimental evidence that the lowest-energy band in the absorption spectrum of $\mathbf{FAAH_2^+}$ is associated to a CT transition.

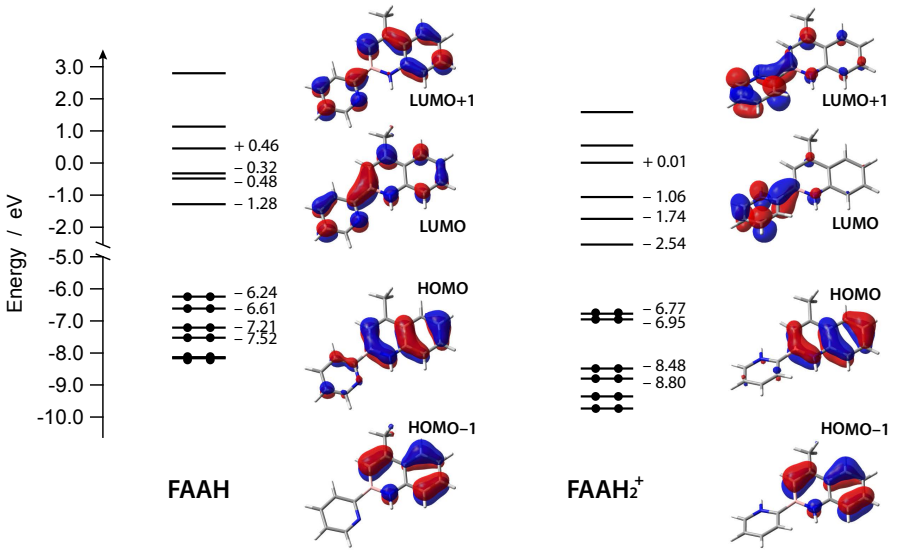

Figure 2.6: Frontier molecular orbitals of the neutral (**FAAH**) and protonated ligand (**FAAH$_2^+$**) displayed at 0.04 $e^{1/2}bohr^{-3/2}$. Orbital energies are provided in eV.

Because the absorption spectrum of **FAAH** displays well-defined vibronic progressions, the vertical excitation energies reported in Table 2.3 are not sufficient to faithfully simulate the experimental absorption spectrum. Consequently, the theoretical absorption spectrum of **FAAH** was calculated taking into account dynamic effects, following a described procedure to compute vibrationally-resolved electronic spectra using Gaussian [32]. Since the highest oscillator strengths for **FAAH** are associated mainly to the transitions from the ground state S_0 to the excited states S_1 and S_4, only the vertical transitions to these two excited states were considered for vibronic calculations. The theoretical and experimental absorption spectra for **FAAH** are reported in Figure 2.7 on the next page.

The obtained theoretical spectrum well-matches the experimental one, especially in the case of the $S_0 \longrightarrow S_1$ vibronic transition, that occurs in the region between 300 nm to 350 nm.

On the contrary, the $S_0 \longrightarrow S_4$ bands do not exactly match the experimental profile, probably due to the overlap with other high-energy transitions. However, the TD-DFT vibronic calculation suggests that the experimentally observed shoulder at 277 nm could arise from the 0-0 absorption maximum of the $S_0 \longrightarrow S_4$ transition (calculated at 275 nm).

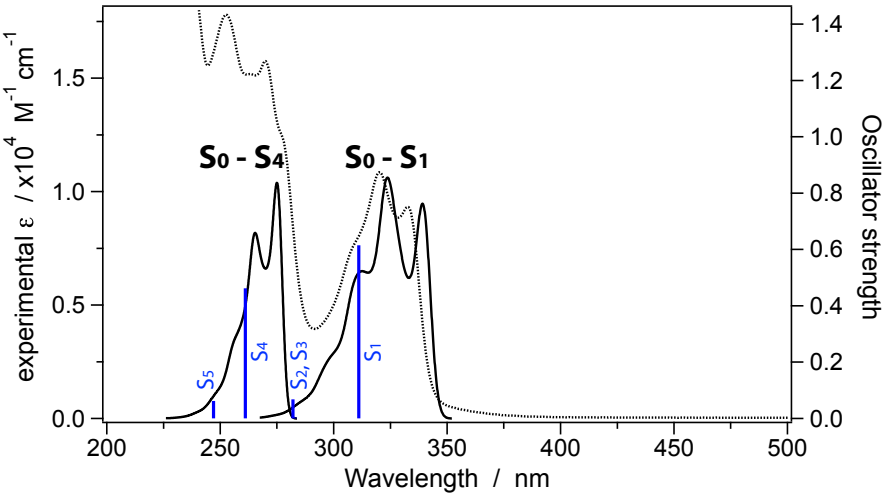

Figure 2.7: Theoretical (full) and experimental (dotted) absorption spectra of **FAAH** in acetonitrile at room temperature. The blue bars represent the oscillator strength calculated for the vertical excitations.

In order to investigate the emission properties of both the neutral and the protonated form of the azaborine ligand, the emission spectrum of **FAAH** was recorded at room temperature in dichloromethane upon titration with trifluoroacetic acid (Figure 2.8 on the following page).

Table 2.4 reports the emission parameters of both **FAAH** and $\mathbf{FAAH_2^+}$ in solution (*i.e.* emission wavelength λ_{ems}, photoluminescence quantum yield Φ, excited-state lifetime τ and kinetic constants associated with radiative (k_r) and non-radiative processes (k_{nr}) for the deactivation of the excited-state).

The emission profiles of **FAAH** and $\mathbf{FAAH_2^+}$ in acetonitrile are not significantly different from the ones in dichloromethane, for this reason they are not reported here, however the emission parameters in acetonitrile can be found in Table 2.4.

While the quantum yield and excited-state lifetime of the neutral **FAAH** in acetonitrile are comparable with the ones measured in dichloromethane, in the

Table 2.4: Emission parameters of **FAAH** and $\mathbf{FAAH_2^+}$ in air-equilibrated solution at room temperature (sh = shoulder).

	solvent	λ_{ems} (nm)	Φ (%)	τ (ns)	k_r ($10^8 s^{-1}$)	k_{nr} ($10^8 s^{-1}$)
FAAH	dichloromethane	348 (sh), 362, 376 (sh)	27.8	1.4	2.0	5.1
	acetonitrile	347 (sh), 358, 372 (sh)	21.5	1.3	1.6	5.9
$\mathbf{FAAH_2^+}$	dichloromethane	480	41.3	3.9	1.1	1.5
	acetonitrile	490	0.9	0.1	0.7	8×10^1

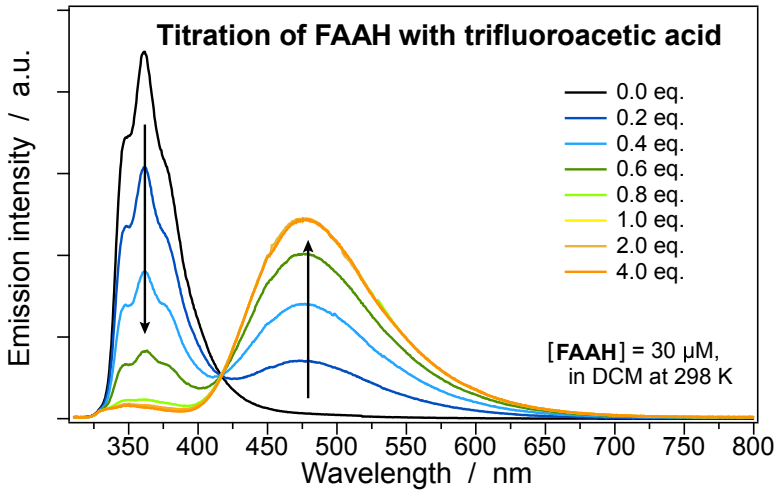

Figure 2.8: Emission spectral changes of **FAAH** upon addition of increasing amounts of trifluoroacetic acid in room-temperature dichloromethane, range between 0 and 4 equivalents.

case of $\mathbf{FAAH_2^+}$ the emission in acetonitrile is much quenched, with a quantum yield <1 %. This difference is definitely to be ascribed to the enhanced non-radiative deactivation (the k_{nr} value increases by more than 50 times in acetonitrile), the reasons for this unexpected photophysical behavior are still under investigation.

Concerning the dichloromethane solutions, the emission band of **FAAH** is well structured and higher in energy compared to that of $\mathbf{FAAH_2^+}$, which displays a broad and unstructured band due to its charge-transfer emitting state. The experimental emission wavelength can be compared with the results of the TD-DFT optimization of the first excited singlet S_1: such theoretical approach gives the expected emission wavelength as the vertical excitation energy in the optimized geometry of S_1. The calculated emission wavelength in acetonitrile in the case of **FAAH** is 352 nm, which is comparable with the energy of the experimentally observed shoulder at 347 nm, ascribable to the 0-0 transition. For what concerns the protonated $\mathbf{FAAH_2^+}$, the theoretical emission wavelength is 439 nm, which is quite different from the experimental result (490 nm) probably due to solvation effects.

The luminescence of the two investigated compounds was also recorded in oxygen-free dichloromethane solution but no significant change was observed. These results, together with the short excited-state lifetimes, are coherent with a spin-allowed transition (*i.e.* fluorescence).

The photoluminescence quantum yield of the free ligand (in dichloromethane solution) is 27.8 %, and it is further increased by protonation (see Table 2.4). Fo-

cusing on the emission parameters in dichloromethane and recalling the equation linking Φ to the kinetic constants of the deactivation processes:

$$\Phi_{em} = \frac{k_r}{k_r + k_{nr}} \tag{2.1}$$

the increase in the quantum yield can be ascribed mainly to the difference in the k_{nr} value. Despite the radiative decay of **FAAH** ($k_r = 2.0 \cdot 10^8 s^{-1}$) is almost twice as fast as in the case of $\mathbf{FAAH_2^+}$ ($k_r = 1.1 \cdot 10^8 s^{-1}$), the non-radiative constant in the neutral ligand ($k_{nr} = 5.1 \cdot 10^8 s^{-1}$) is more than three times grater than in the protonated form ($k_{nr} = 1.5 \cdot 10^8 s^{-1}$) and this significantly lowers the luminescence efficiency. Comparing the results in the two different solvents, the k_r value is almost halved when passing from dichloromethane to acetonitrile for both **FAAH** and $\mathbf{FAAH_2^+}$, while the k_{nr} is more variable, especially in the case of $\mathbf{FAAH_2^+}$ for which the k_{nr} in acetonitrile is more than fifty times grater than that in dichloromethane due to the quenching phenomena mentioned above.

The Stokes' shift (*i.e.* the energy difference between the absorption and the emission bands associated to the S_0-S_1 transitions) is a useful parameter that gives information about the geometrical distortion of the excited state. After excitation, the molecules undergo both vibrational relaxation (to reach the lowest vibrational level of S_1), and geometrical relaxation (to reach the minimum-energy conformation of the excited state). In the case shown in Figure 2.9 b the excited-state geometrical distortion is almost zero. As a result, the absorption and the emission maxima are both associated to the 0-0 transition and the Stokes' shift is low.

On the contrary, when the excited state is much distorted (as depicted in Figure 2.9 a) the 0-0 transition becomes less probable and the emission maximum is found at significantly lower energy than the absorption maximum (*i.e.* grater Stokes' shift).

Table 2.5 reports the Stokes' shift of **FAAH** and $\mathbf{FAAH_2^+}$ in acetonitrile and in dichloromethane solution at room temperature (the energy difference was calculated between the absorption maximum associated with the $S_0 \rightarrow S_1$ transition and the emission maximum). **FAAH** displays a low Stokes' shift, which means that the minimum-energy geometry of S_1 is similar to that of S_0. The fact that the Stokes' shift is also solvent independent means that the emitting state has a low CT character.

Table 2.5: Stokes' shift of **FAAH** and $\mathbf{FAAH_2^+}$ in acetonitrile and in dichloromethane solution at 298 K.

	Stokes' shift (eV) in dichloromethane	Stokes' shift (eV) in acetonitrile
FAAH	0.42	0.41
$\mathbf{FAAH_2^+}$	0.98	1.17

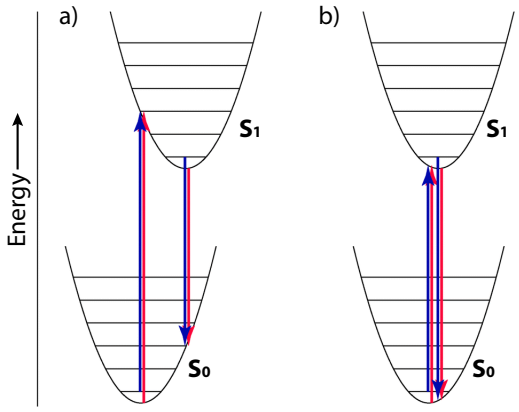

Figure 2.9: Potential-energy diagram for two cases of excited-state distortion: (a) non-zero distortion resulting in a large Stokes' shift, (b) almost no distortion, resulting in a small Stokes' shift [33].

On the contrary the Stokes' shift of the protonated species **FAAH$_2^+$** is much grater (almost 1 eV), meaning that the excited state is highly distorted with respect to S_0. This is in agreement with an emitting state with a high charge-transfer character, since the intramolecular electron transfer can significantly alter the bond lengths and angles.

The DFT-optimized structures of the singlet ground state (S_0) and the first excited singlet (S_1) of **FAAH** and **FAAH$_2^+$** is represented in Figure 2.10 on the facing page; selected bond lengths and dihedral angles are also given.

In the case of **FAAH** the emitting state S_1 does not display a significant geometrical distortion, in agreement with the small experimental Stokes's shift. Both in the ground and in the excited state the molecule is kept perfectly planar by the NH−N hydrogen bonding. The B−C bond connecting the borazaronaphthalene and the pyridine moieties shortens passing from S_0 to S_1 because of the population of LUMO, which has a bonding character along this specific connection (see Figure 2.6 on page 26).

On the contrary, **FAAH$_2^+$** is characterized by a geometrically-distorted emitting state, as expected from the great Stokes' shift. Notably, in its ground state, **FAAH$_2^+$** is not planar but the dihedral angle between the borazaronaphthalene plane and the pyridine plane (ϕ) is 153.3° to minimize the sterical interaction. In this case, when the LUMO is populated upon excitation, not only the B−C bond is shortened, but also the molecule becomes planar (ϕ = 180.0°) to maximize the π interaction of the LUMO.

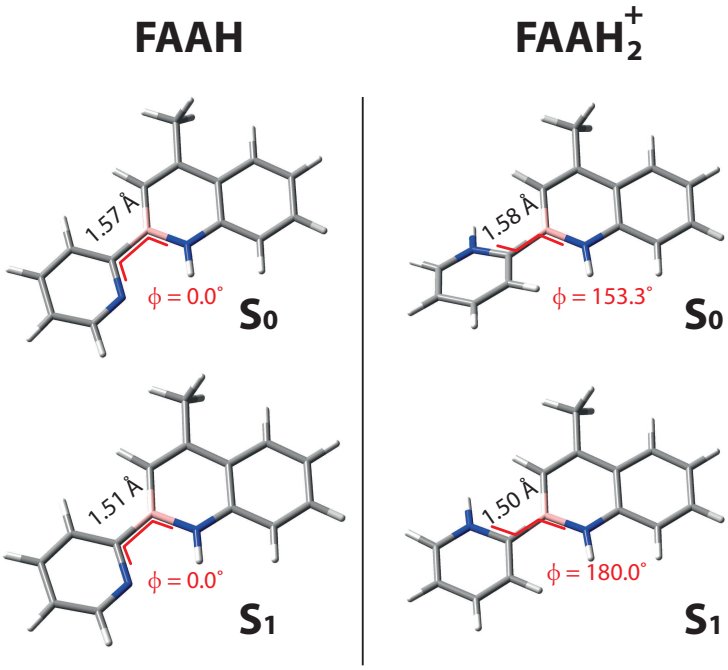

Figure 2.10: DFT-optimized geometries of **FAAH** and **FAAH$_2^+$** in the ground state S_0 and in the first excited singlet S_1. The length of the B—C bond connecting the borazaronaphthalene unit to the pyridine moiety (black), as well as the dihedral angle between the borazaronaphthalene plane and the pyridine plane (ϕ, red) are given.

The emission spectra of **FAAH** and **FAAH$_2^+$** were also recorded in a frozen butyronitrile glass at 77 K. At low temperature these molecules display both fluorescence and phosphorescence (at longer wavelengths). The emission spectra at 298 K (in dichloromethane) and 77 K are depicted in Figure 2.11 on the following page, while Table 2.6 reports the emission wavelength and excited-state lifetime of both the fluorescence and the phosphorescence at 77 K.

The fluorescence of **FAAH** becomes more structured at low temperature, but the emission maximum is rather unchanged. The phosphorescence of **FAAH** is much structured and it is quite different from its fluorescence in terms of energy. The phosphorescence excited-state lifetime is very long (2.68 s), as commonly observed for purely organic molecules.

In the case of **FAAH$_2^+$**, the fluorescence at low temperature still exhibits a broad and unstructured profile, but the emission maximum is much blue-shifted at 77 K due to rigidochromic effects. These observations confirm the CT nature of the emitting state. The phosphorescence of the protonated species is a bit structured but still broad, and it is quite close in energy to the relative fluorescence.

Comparing the fluorescence parameters of **FAAH** and **FAAH$_2^+$** at room tem-

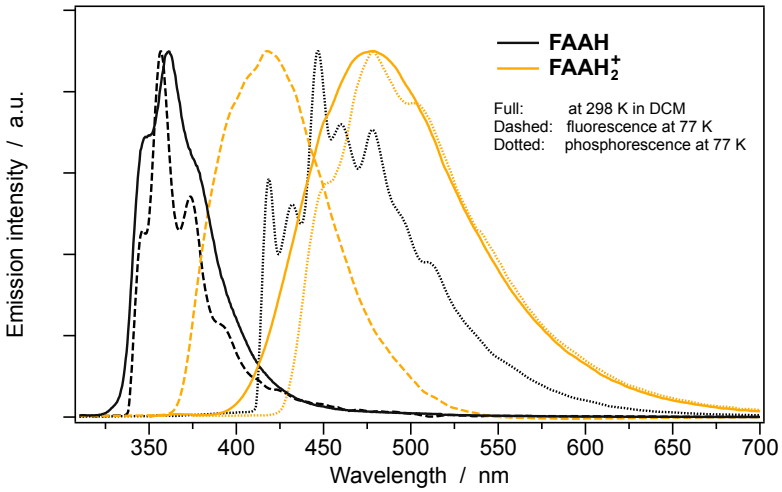

Figure 2.11: Fluorescence and phosphorescence of **FAAH** and **FAAH$_2^+$**.

Table 2.6: Emission parameters of **FAAH** and **FAAH$_2^+$** in frozen butyronitrile glass at 77 K (sh = shoulder)

	emitting state	λ_{ems} (nm)	τ
FAAH	S_1	347 (sh), 357, 374, 391 (sh), 422 (sh)	2.32 ns
	T_1	418, 432, 447, 460, 478, 439 (sh), 510 (sh)	2.68 s
FAAH$_2^+$	S_1	417	4.12 ns
	T_1	452 (sh), 478, 502 (sh)	1.52 s

perature with those measured at 77 K, it is also possible to appreciate a significant increase in the excited-state lifetime at low temperature, as expected when passing from solution to a rigid matrix (see Tables 2.4 and 2.6 for comparison). It should be noted that relative increase in the case of **FAAH** is much grater than that of **FAAH$_2^+$** (*i.e.* τ of **FAAH** is raised by more than 60% at low temperature, while τ of **FAAH$_2^+$** only increases by about 6% passing from the dichloromethane solution to the butyronitrile glass). This is probably because the non-radiative deactivation processes (that were particularly fast in the case of **FAAH** at room temperature) are much reduced in the rigid matrix at low temperature, thus increasing the excited-state lifetime.

In order to assess the nature of the experimentally observed phosphorescence, unrestricted DFT calculations were performed on the lowest energy triplet state of both **FAAH** and **FAAH$_2^+$**; the relative spin density distributions are reported in Figure 2.12 on the next page.

In the case of the protonated **FAAH$_2^+$**, the spin density distribution well matches the topology of the HOMO⟶LUMO excitation (see Figure 2.6 on page 26) and

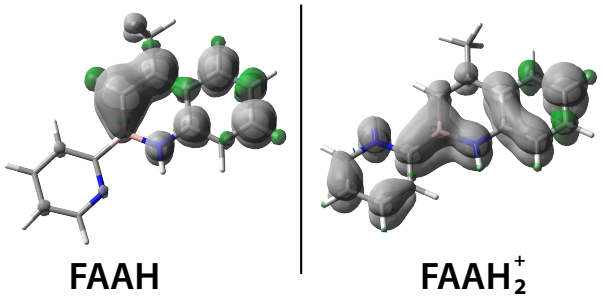

Figure 2.12: Spin density distribution ($0.002\,e\,bohr^{-3}$) of the T_1 state for **FAAH** and **FAAH**$_2^+$.

confirms the CT nature of the excited state also for T_1. On the other hand, the spin density of the lowest triplet state of **FAAH** is fully centered on the borazaronaphthalene moiety and does not match the HOMO→LUMO excitation associated with the first excited singlet S_1: this difference between the emitting states is in agreement with the large experimental energy gap between the fluorescence and the phosphorescence bands of **FAAH**.

From the DFT calculations it is also possible to obtain an estimate of the phosphorescence emission wavelength as the adiabatic energy difference between T_1 and S_0 in their minimum-energy point. In the case of **FAAH** the minimum of T_1 is estimated 2.97 eV above S_0 which corresponds to 417 nm: this well-matches the first experimental peak at 418 nm ascribable to the 0-0 transition. For what concerns **FAAH**$_2^+$ the calculated minimum-energy configuration of T_1 is 2.63 eV above S_0 which corresponds to 471 nm, which is comparable to the experimental emission maximum at 478 nm.

2.4.2 Iridium(III) complexes

The Iridium(III) complexes were characterized both in solution and in solid state (*i.e.* frozen butyronitrile glass at 77 K and doped-PMMA films). The singlet ground state (S_0) and the lowest triplet states of interest (*vide infra*) were optimized by means of theoretical calculations as described in the computational details.

In the case of **FAB** , it was not possible to carry out the emission measurements in solution at 298 K because the complex was not stable over the period of time required to prepare the sample (*i.e.* adjusting the sample absorbance, bubbling Argon for 30 min to remove oxygen) hence, some spurious emissions were observed due to degradation and it was not possible to obtain reliable results. The same problem was found in the case of the PMMA film doped with **FAB** , since the drop-casting procedure requires some time for the evaporation of the solvent. For these reasons, here we only report **FAB** 's room-temperature absorption spectra in solution, which were recorded right after the dissolution of the complex, and its emission parameters in butyronitrile glass, since the solution was immediately frozen at 77 K.

The room temperature electronic absorption spectra of the three Ir(III) complexes in solution are reported in Figure 2.13, and the relative absorption maxima are reported in Table 2.7 on page 36.

The absorption spectra of **FAV** and **FAB** display a similar profile, despite the spectrum of **FAB** is blue shifted compared to **FAV** , due to the electron-withdrawing effect of the fluorine substituents on the cyclometalating ligands of the former. On the contrary, the spectrum of **FAR** displays a different profile and it is also the most red-shifted of the series. For the three complexes, the intense bands between 200 and 300 nm ($\epsilon > 2 \times 10^4\,M^{-1}cm^{-1}$) are assigned to spin-allowed ligand centered (LC) $\pi - \pi^*$ transitions. The interpretation of the less intense and broader bands found at longer wavelengths is not trivial, therefore we compared the experimental spectra with TD-DFT calculated ones (see Figures 2.14, 2.15 and 2.16).

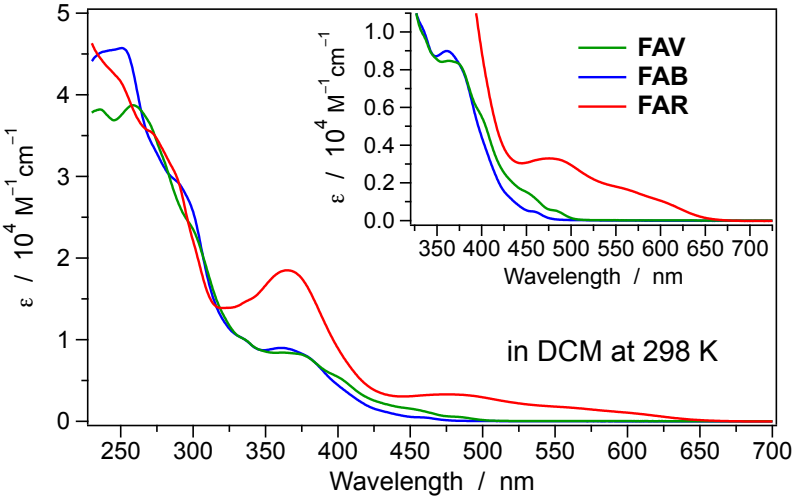

(a) in dicloromethane at 298 K

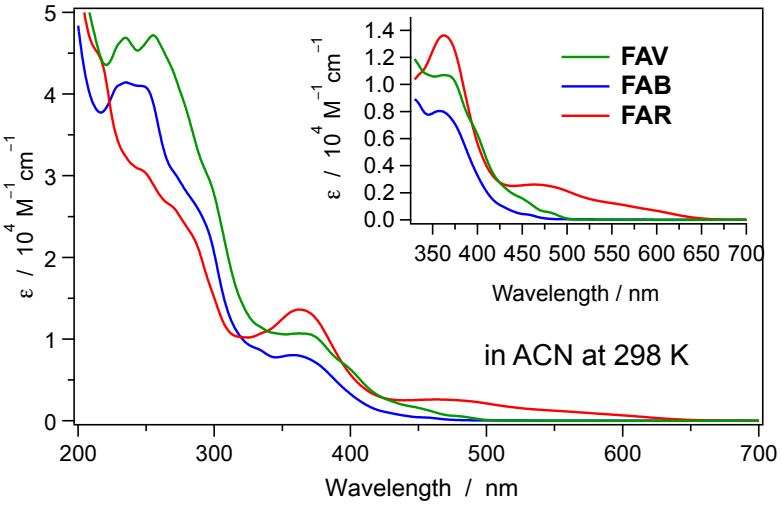

(b) in acetonitrile at 298 K

Figure 2.13: Absorption spectra of **FAV** , **FAB** and **FAR** in solution at 298 K

Table 2.7: Absorption maxima of **FAV** , **FAB** and **FAR** in solution at 298 K (sh = shoulder, ACN = acetonitrile, DCM = dichloromethane)

	FAV		**FAB**		**FAR**	
	λ_{max} (nm)	ϵ ($\cdot 10^4$ $M^{-1}cm^{-1}$)	λ_{max} (nm)	ϵ ($\cdot 10^4$ $M^{-1}cm^{-1}$)	λ_{max} (nm)	ϵ ($\cdot 10^4$ $M^{-1}cm^{-1}$)
ACN	480 (sh)	0.06	456 (sh)	0.04	560 (sh)	0.11
	447 (sh)	0.17	359	0.80	464	0.26
	396 (sh)	0.69	332 (sh)	0.88	362	1.36
	366	1.07	285 (sh)	2.67	268 (sh)	2.63
	295 (sh)	3.00	248	4.09	245 (sh)	3.08
	255	4.72	235	4.14	213 (sh)	4.54
	234	4.69				
DCM	484 (sh)	0.05	460 (sh)	0.05	557 (sh)	0.18
	450 (sh)	0.15	362	0.90	475	0.33
	399 (sh)	0.56	335 (sh)	1.01	365	1.85
	363	0.85	292 (sh)	2.88	271 (sh)	3.55
	335 (sh)	1.01	251	4.57	245 (sh)	4.26
	298 (sh)	2.42				
	259	3.87				
	236	3.82				

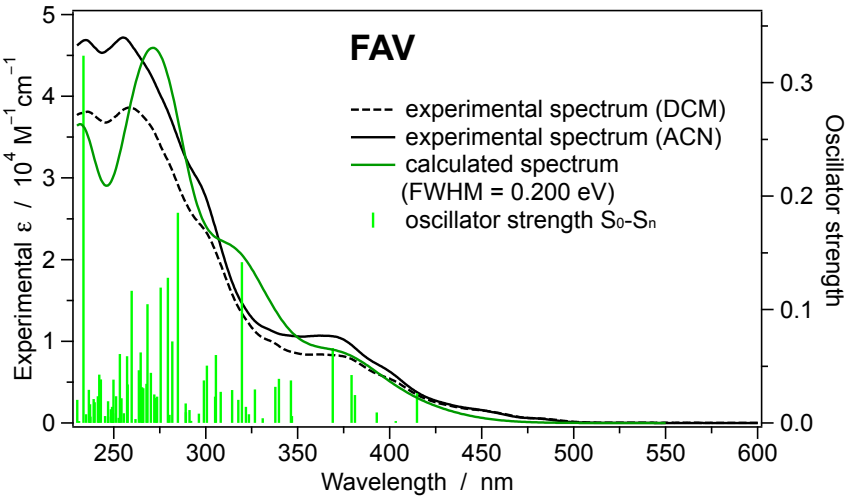

Figure 2.14: TD-DFT calculated absorption spectrum in acetonitrile of **FAV** compared with experimental absorption spectra at room temperature.

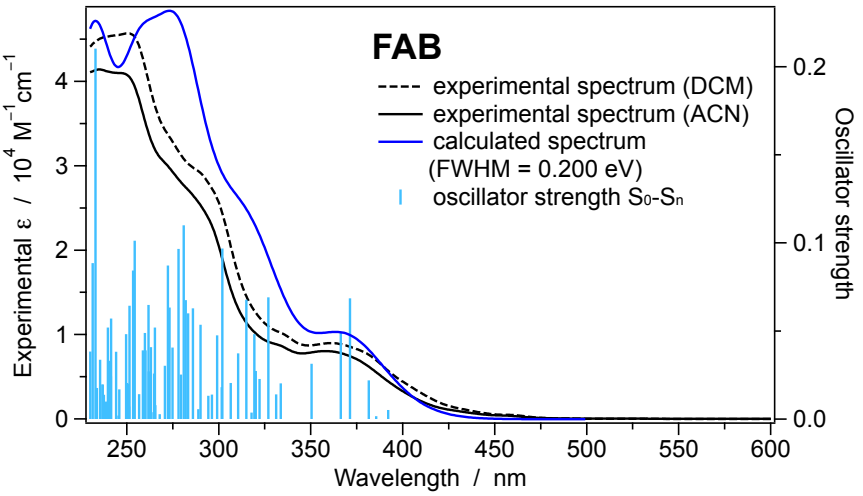

Figure 2.15: TD-DFT calculated absorption spectrum in acetonitrile of **FAB** compared with experimental absorption spectra at room temperature.

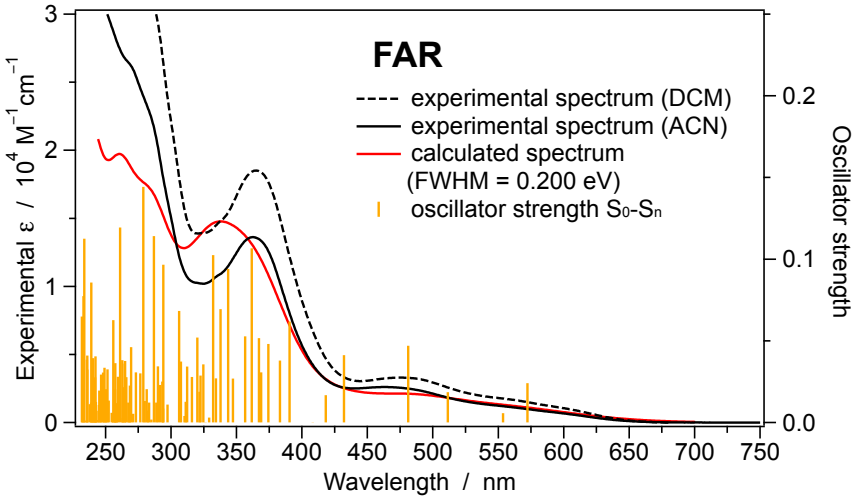

Figure 2.16: TD-DFT calculated absorption spectrum in acetonitrile of **FAR** compared with experimental absorption spectra at room temperature.

In all of the cases the profile of the calculated spectrum well-matches the experimental result, especially for what concerns the absorption bands below 350 nm, while the energy of the intense bands found at shorter wavelengths is a bit underestimated by the TD-DFT prediction. All the three complexes display an absorption maximum around 360 nm (see Table 2.7 on page 36). In the case of both **FAV** and **FAB** the TD-DFT calculations suggest that this band is associated with the vertical excitations from S_0 to the excited states S_4, S_5 and S_6, with oscillator strengths ranging from 0.04 to 0.07. A straightforward attribution of these transitions is not easy, since they all display a high multiconfigurational character with several contributions from different monoexcitations (*i.e.* from the HOMO or HOMO-1 to the empty LUMO, LUMO+1 or LUMO+2, with relative weight from about 30 to 50 %). The involved frontier molecular orbitals of **FAV** e **FAB** display a virtually identical topology (see Figure 2.17 on the next page). All the occupied orbitals involve the borazaronaphthalene unit (HOMO) and the two cyclometalating moieties of the C^N ligands (HOMO-1), with a high contribution form the iridium d orbitals. On the contrary, the unoccupied orbitals are always centered on the pyridine units of the three ligands. Consequently, to keep it simple, they can all be classified as MLCT transitions (with different admixture of ligand-centered and intra-ligand nature), which explains their low oscillator strengths.

In the case of **FAR** , the absorption peak around 360 nm is mainly ascribable to the vertical excitations from S_0 to the excited states S_{16} and S_{19}, with oscillator strengths around 0.1. These excitations involve transitions centered on one of the two quinoxaline ligands, with a minor MLCT contribution. As a consequence, in this spectral region, **FAR** displays absorption bands with higher epsilon, compared to **FAV** and **FAB** , due to the major LC nature.

Concerning the $S_0 \longrightarrow S_1$ transition, the DFT calculations suggest that there is a contribution of the HOMO⟶LUMO monoexcitation for all the three complexes, but with a different relative weight. In all the investigated complexes, the HOMO is centered on the azaborine ligand (with some contribution from the Iridium d orbitals), while the LUMO is basically centered on the nitrogen-containing moiety of one of the C^N ligands. In the case of both **FAB** and **FAR** the HOMO⟶LUMO is the main monoexcitation (with a relative weight of about 60 %), while in the case of **FAV** , the main contribution to the population of S_1 is from the HOMO-1⟶LUMO excitation (60 %), with a minor contribution of the HOMO⟶LUMO monoexcitation (24 %).

The weak bands experimentally observed below the $S_0 \longrightarrow S_1$ transition are ascribable to direct population of the lowest triplet states, favored by the strong spin-orbit coupling of the Iridium center. Accordingly, TD-DFT calculated vertical excitations from the ground state to the lowest triplet states T_1, T_2 and T_3 are found at lower energy than the $S_0 \longrightarrow S_1$ band (see Table 2.8 on the facing page). Looking at the inset showing a close-up of the low-energy bands in the absorp-

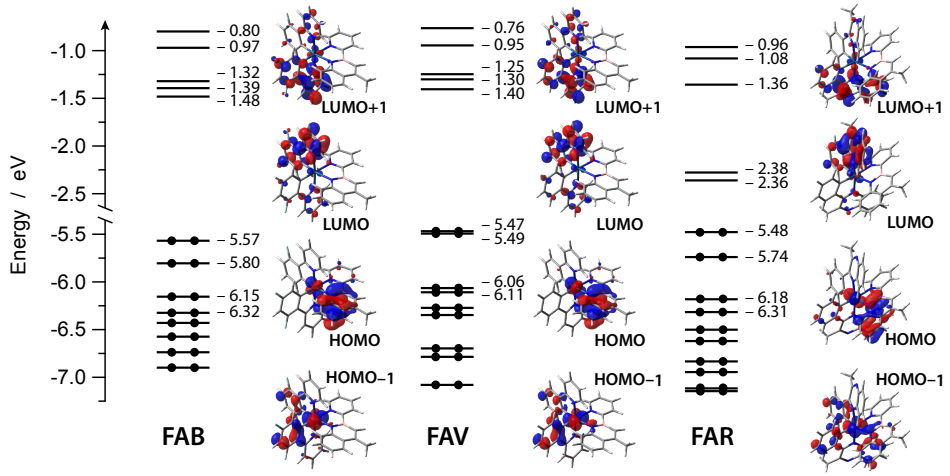

Figure 2.17: Frontier molecular orbitals of **FAV** , **FAB** and **FAR** in acetonitrile displayed at 0.04 $e^{1/2}bohr^{-3/2}$. Orbital energies are provided in eV.

Table 2.8: Vertical excitations energies from the ground state S_0 to the first excited singlet S_1 and the lowest triplets T_1, T_2 and T_3

	$S_0 \rightarrow S_1$		$S_0 \rightarrow T_1$		$S_0 \rightarrow T_2$		$S_0 \rightarrow T_3$	
	eV	nm	eV	nm	eV	nm	eV	nm
FAV	2.99	415	2.67	465	2.70	460	2.70	459
FAB	3.16	392	2.72	456	2.83	438	2.84	436
FAR	2.17	572	1.97	630	2.05	605	2.09	594

tion spectra of the complexes in acetonitrile (Figure 2.13 (b)), it is even possible to identify the $S_0 \rightarrow T_1$ transition in the spectra of **FAV** and **FAB** as a shoulder visible at 480 and 456 nm respectively.

TD-DFT calculations indicate that the vertical transitions to the lowest triplets are strongly multiconfigurational and can be hardly visualized in terms of compact series of occupied/virtual Kohn-Sham molecular orbitals couples. For this reason we performed a Natural Transition Orbital (NTO) analysis, which gives an easier description of the associated electronic excitations [34]. Figure 2.18 on page 41 represents the $S_0 \rightarrow T_n$ transition (n = 1, 2, 3) in terms of NTOs couples for all the investigated complexes.

In the case of **FAV** the excitations associated with the $S_0 \rightarrow T_1$ and $S_0 \rightarrow T_2$ transitions are almost centered on the two cyclometalating ligands (from the Iridium d orbitals and the orbitals of the phenyl moiety of a C^N ligand to the π^* orbitals of pyridine moiety of the same C^N ligand). On the other hand, the transition from S_0 to T_3 involves an electronic excitation centered on the azaborine ligand, and the involved NTOs resemble the HOMO and LUMO of the free ligand **FAAH** (see Fig-

ure 2.6 on page 26). The considered vertical excitations are very close in energy, with T_1 standing just 0.03 eV below the virtually isoenergetic T_2 and T_3.

The lowest three triplet states of **FAB** are essentially the same of **FAV** (similar NTOs, see Figure 2.18), but their energy ordering is different: the excited states centered on the cyclometalating ligands are now higher in energy compared to the triplet state centered on the azaborine ligand. This is due to the effect of the fluorine substituents, which stabilize the π orbitals of the phenyl rings of the cyclometalating ligands, increasing the energy of the associated transitions.

The scenario is much different in the case of **FAR** . Here, the $S_0 \longrightarrow T_1$ transition is achieved by the promotion of one electron from the d orbitals of the metal center and π orbitals of both the azaborine and one quinoxaline, to the π^* orbitals of the same cyclometalating ligand. Hence, T_1 has a mixed MLCT/LLCT/LC character. Instead, T_2 is basically centered on one quinoxaline ligand, with a small contribution from Iridium d orbitals. Eventually, T_3 is LLCT/MLCT in character, since it can be populated by the promotion of one electron from the iridium d orbitals and the azaborine π orbitals to one quinoxaline π^* orbital.

Since the emission of Iridium complexes is expected from the lowest triplet state, we can expect that:

i) in the case of **FAV** the emitting state will probably be centered on one of the cyclometalating ligands, even if this prediction should be carefully verified taking into account excited-state relaxation effects, since the three lowest triplet are very close in energy;

ii) in the case of **FAB** the emission is expected from a triplet state centered on the azaborine ligand, since the LC states centred on the C^N ligands are rather high in energy compared to T_1;

iii) the emission of **FAR** is expected from a state which is quite heterogeneous in nature (MLCT/LLCT/LC).

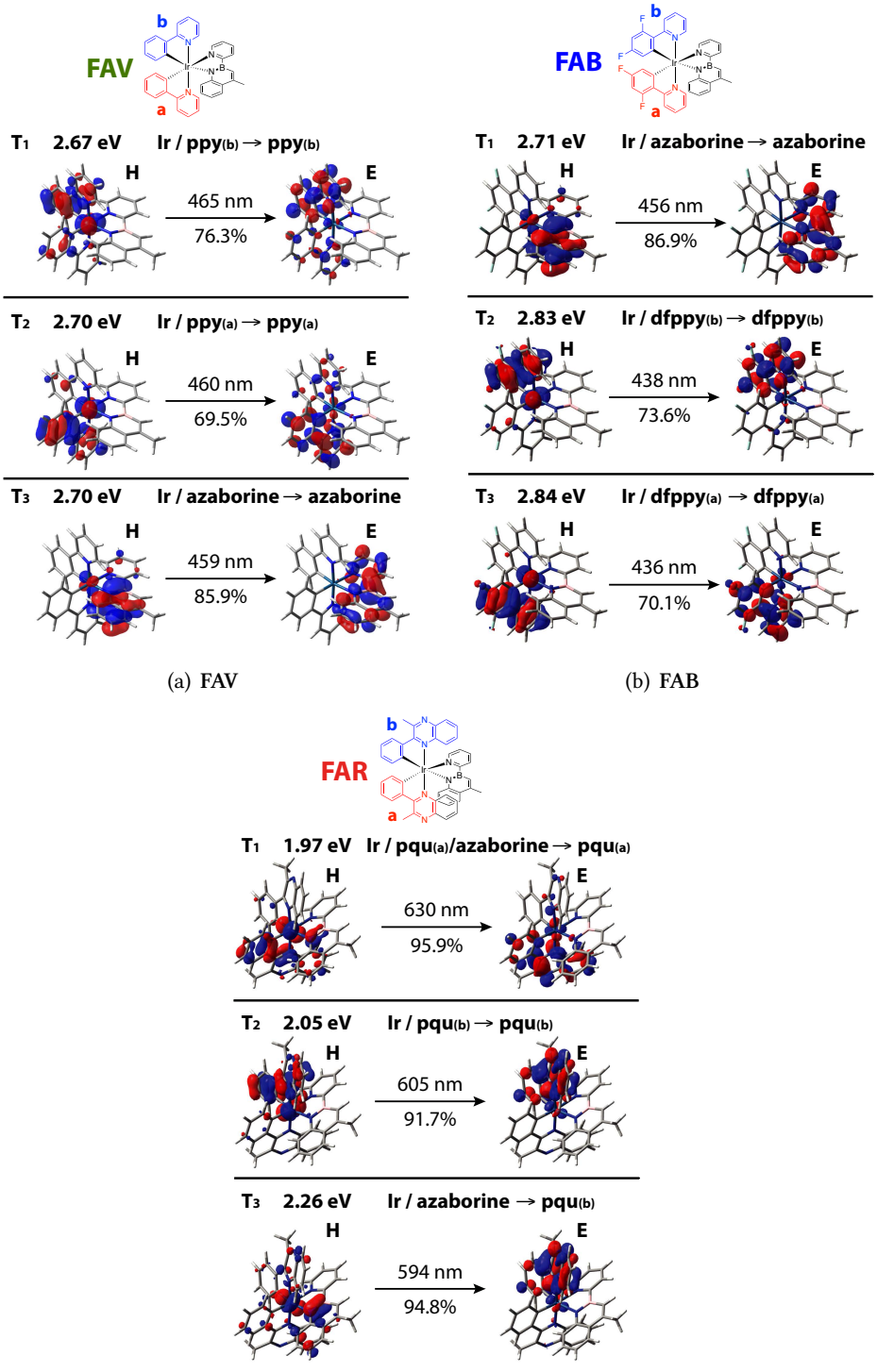

(a) FAV

(b) FAB

(c) FAR

Figure 2.18: Natural Transition Orbitals associated with the $S_0 \rightarrow T_n$ transition (n = 1, 2, 3) for the Iridium complexes (H = hole, E = electron). The contribution of the represented excitation is also given as a percentage.

The experimental emission spectra in dichloromethane of **FAV**, **FAB** and **FAR** are reported in Figure 2.19 on the next page, in dichloromethane at room temperature, in PMMA film (1 % w/w) and at 77 K (the emission spectra in acetonitrile solution are virtually identical to those recorded in dichloromethane and are not reported); Table 2.9 collects the luminescence properties in both solvents. The spectra in solution refer to oxygen-free samples.

The emission spectrum of **FAV** at room temperature is almost identical both in solution and in PMMA. Anyway, both the quantum yield and the excited-state lifetime increase passing from solution to polymer matrix, probably due to the reduction in vibrational deactivations (as confirmed by the dramatic decrease of k_{nr} in PMMA compared to the solution, see Table 2.9). At low temperature the emission profile of **FAV** becomes more structured, but it preserves the same emission onset, confirming the expected LC nature of T_1.

The only available emission spectrum of **FAB** is the one at 77 K (see above). Its emission profile is structured as well, and it resembles that of **FAV** under the same experimental conditions, both in terms of profile and emission wavelength; only a minor blue shift of about 10 nm is observed. This evidence suggests that the phosphorescence of these two complexes comes from similar emitting states.

Concerning complex **FAR**, the broad and unstructured emission band observed under all the experimental conditions suggests that the emitting state has a significant charge-transfer character. This hypothesis is further corroborated by the shift of the emission maximum under the different experimental conditions (see Table 2.9). The hypsochromic shift observed in PMMA and at 77 K is typical of ^{3}MLCT states and it is referred to as "rigidochromism" [35]: due to its charge-transfer nature, the excited state will posses a different dipole moment than the ground state, and will be destabilized until the dipole moments of the surrounding environment (*i.e* the solvent molecules) are able to reorient and facilitate a more favorable electrostatic interaction. In a rigid matrix (*i.e.* PMMA or frozen solvent at 77 K), the motion of the surrounding molecules will be so restrained that

Table 2.9: Emission properties of **FAR**, **FAB** and **FAR** under different experimental conditions (temperature = 298 K if not specified).

	experimental conditions	λ_{ems} (nm)	Φ (%)	τ (µs)	k_r ($10^5 s^{-1}$)	k_{nr} ($10^5 s^{-1}$)
FAV	acetonitrile	516	21.5	1.7	1.2	4.5
	dichloromethane	510	30.4	1.4	2.1	4.9
	PMMA	513	67.4	3.5	1.9	0.9
	at 77 K	490, 526, 566	-	9.4	-	-
FAB	at 77 K	484, 516, 556, 598 (sh)	-	19.8	-	-
FAR	acetonitrile	714	4.4	1.6	0.3	5.8
	dichloromethane	703	7.4	1.6	0.5	5.8
	PMMA	682	22.3	1.3	1.7	6.0
	at 77 K	663	-	10.1	-	-

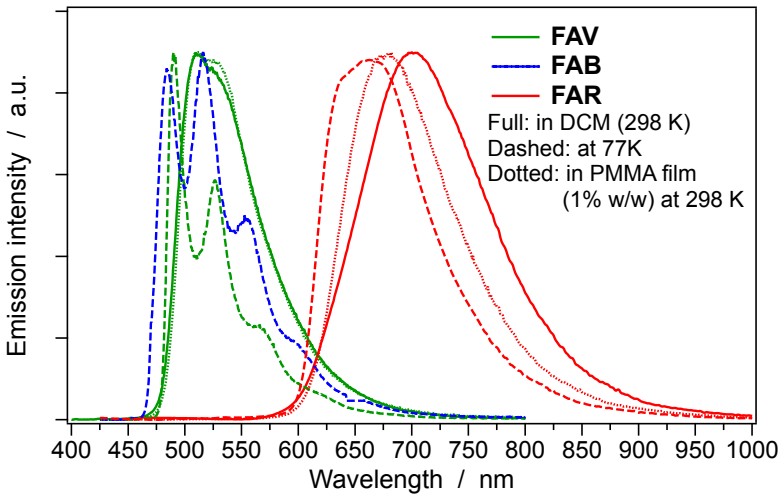

Figure 2.19: Corrected and normalized emission spectra of **FAV**, **FAB** and **FAR** in dichloromethane at 298 K, in PMMA film (1 % w/w) at room temperature and at 77 K.

they will be unable to effectively reorient themselves around the ^{3}MLCT excited molecule. As a consequence, the ^{3}MLCT excited state will be destabilized and the observed emission wavelength will be blue shifted.

The luminescence quantum yield in solution of **FAR** is not very high (7.4 % and 4.4 % in dichloromethane and acetonitrile, respectively), probably due to both the energy-gap law and the distorted excited-state geometry of the bulky quinoxaline ligands. The emission parameters of **FAR** in PMMA are significantly different from those in solution: the quantum yield is much higher (Φ_{PMMA}= 22.3 %), but this is not the case of the excited-state lifetime, which remains similar to the one measured in solution (see Table 2.9). As a consequence, the k_r in PMMA is one order of magnitude grater than the k_r in solution, which suggest that the emitting state could not be the same under the two experimental conditions.

In order to get a deeper insight on the emitting state of all the investigated complexes, TD-DFT optimizations were carried out on the three lowest triplet states of each complex (*i.e.* the T_1, T_2 and T_3 discussed above), starting from the Franck-Condon region. The main target of this approach is to take into account relaxation effects, to check the occurrance of excited-state flipping and eventually identify the final emitting state.

In Figure 2.20 (a) are depicted the spin density distributions and the relative energy of T_1, T_2 and T_3 of complex **FAV** in acetonitrile, in their minimum energy conformation. Notably, after full geometry relaxation, the energy ordering of these three states is different from the one found by the vertical-excitation cal-

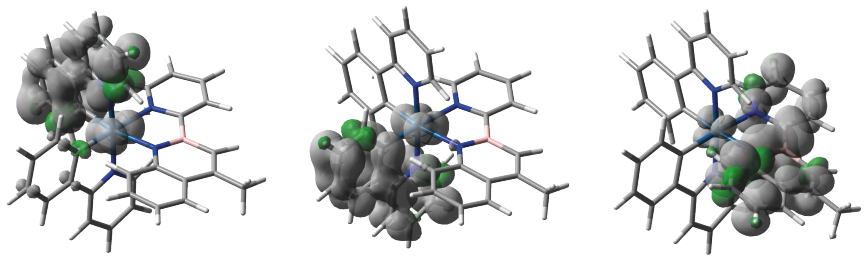

(a) **FAV**

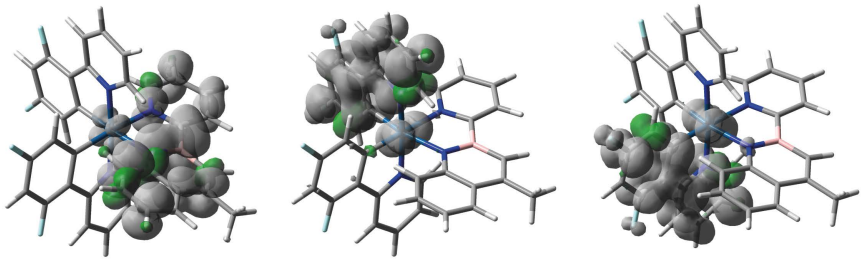

(b) **FAB**

Figure 2.20: Spin density distribution (0.002 e bohr^{-3}) for the optimized triplets T_1, T_2 and T_3 of complexes **FAV** and **FAB** computed in acetonitrile; the optimized energy of each excited state is also given, relative to the lowest triplet.

culation in the S_0 minimum geometry. The lowest triplet turns out to be the one centered on the azaborine ligand (*i.e.* the "old" T_3, see Figure 2.21 on the facing page).

Concerning complex **FAB** (Figure 2.20 (b)), the energy ordering of the three triplets is manteined after relaxation, and the lowest triplet state remains the one centered on the azaborine ligand (*i.e.* T_1). This was an expected result, since T_1 was significantly lower in energy compared to T_2 and T_3 even at the geometry of S_0. To sum up, we can say that the lowest triplet state (*i.e.* the emitting state) is the same in the case of **FAV** and **FAB** and it is centered on the azaborine ligand. This result is in accordance with the experimental evidence that the two mentioned complexes display a similar emission spectrum at 77 K, both in terms of vibronic progression and energy. The adiabatic energy difference between the lowest triplet and the ground state is calculated to be 2.51 eV for **FAV** and 2.53 eV for **FAB** , which correspond to an emission wavelength of 494 nm and 490 nm respectively. This is in good agreement with the experimental energy of the first

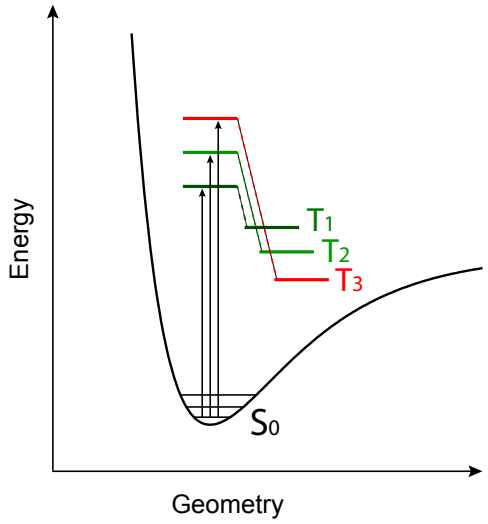

Figure 2.21: Schematic representation of root flipping in the case of **FAV**. The energy ordering of the triplet states changes upon geometry relaxation and the "old" T_3 becomes the lowest triplet state.

peak in the emission spectra of these compounds at 77 K (**FAV** : 490 nm = 2.53 eV; **FAB** : 484 nm = 2.56 eV).

To get a further proof that the emitting states of **FAV** and **FAB** are both centered on the azaborine ligand, we analyzed the vibrational progression of their spectra at 77 K and compared it with that of the phosphorescence of the free ligand **FAAH** (see Figure 2.11 on page 32). Such analysis was performed by fitting the spectra using a Meyer function with two frequency components (named hw1 and hw2 respectively) [36]; the results of the fitting are reported in Figure 2.22 on the following page. In all cases, the fitted frequency values are somehow comparable, especially if we consider that this fitting is only a rough approximation of the real vibrational frequencies. In addition, we have to take into account that the vibrational modes of the free azaborine **FAAH** are of course different from the ones that the same ligand can display when coordinated to the Iridium ion. In this context, the results of the fitting can be considered as a further evidence that the emitting state of both **FAV** and **FAB** is LC in nature, centered on the azaborine ligand.

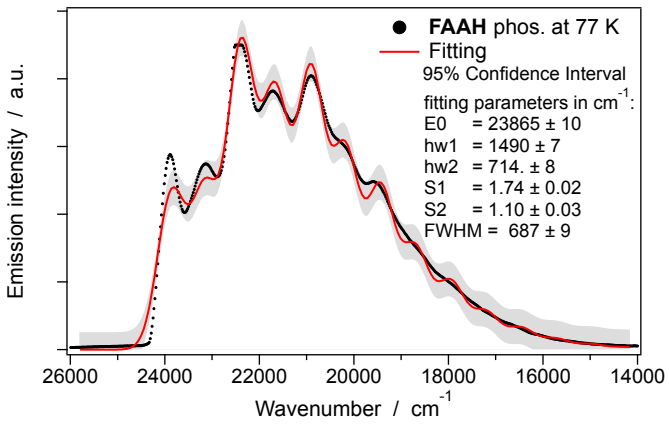

(a) **FAAH**

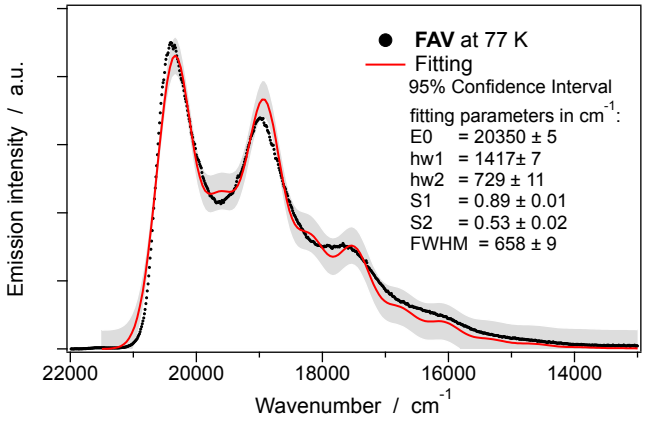

(b) **FAV**

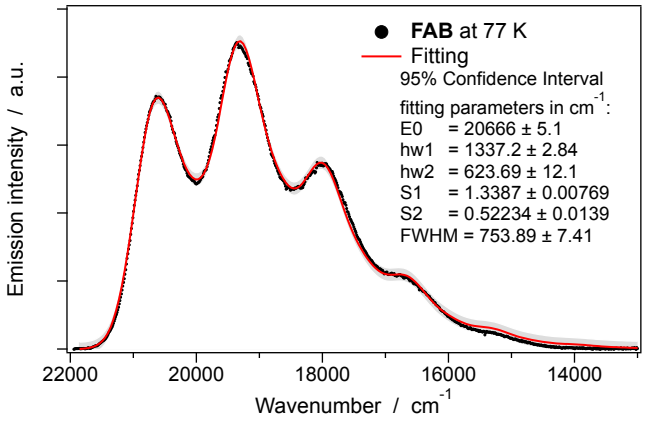

(c) **FAB**

Figure 2.22: Fitting of the phosphorescence of the free ligand **FAAH** and of complexes **FAV** and **FAB** at 77 K using a Meyer function with two frequency components. The fitting parameters are reported in the legend.

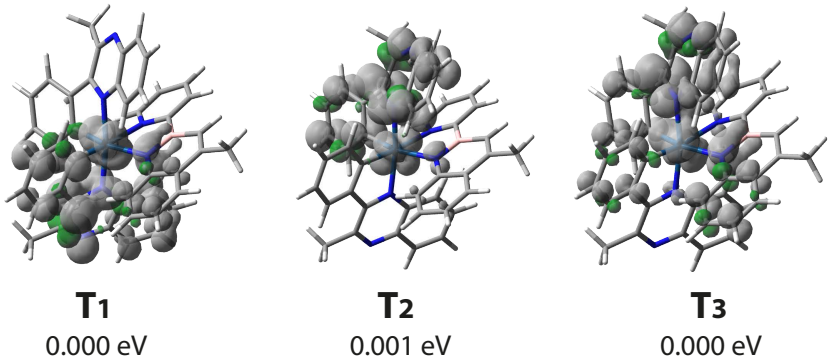

Figure 2.23: Spin density distribution (0.002 e bohr^{-3}) for the optimized triplets T_1, T_2 and T_3 of complex **FAR** computed in acetonitrile; the optimized energy of each excited state is also given, relative to the lowest triplet.

Figure 2.23 collects the spin density distributions and the relative energy of T_1, T_2 and T_3 of complex **FAR**, in their minimum energy conformation. Upon geometry relaxation, the three excited states turned out to be virtually isoenergetic, with T_2 standing only 0.001 eV above T_1 and T_3. The identification of the final emitting state is, therefore, non-trivial; however, we can reasonably say that the emission of **FAR** arises from a ^{3}MLCT state (*i.e.* T_1 or T_2, see Figure 2.18 on page 41), since the observed emission band is broad and unstructured.

As discussed above, the emission parameters of **FAR** in PMMA are surprisingly different from those in solution, in particular for what concerns the k_r value, which undergoes a dramatic increase in the polymer matrix (see Table 2.9 on page 42). Since k_r is an intrinsic property of the emitting state, its significant change in PMMA matrix suggests that the emission could arise from a different excited state, respect to the solution. The energy-proximity of the three excited states is probably responsible for this phenomenon: the restrained geometry relaxation in rigid matrix (*i.e.* PMMA) could alter the triplet energy levels compared to the solution, resulting in a probable change in the emitting state (*i.e.* the lowest triplet state).

Chapter 3

Conclusions

The synthesis of a novel heteroaromatic compound (**FAAH**) belonging to the class of 1,2-azaborines has been reported. The associated reaction yield is not high, however it was possible to isolate and characterize compound **FAAH** by means of NMR spectroscopy. The mentioned borazaro compound was then used as an anionic ligand (upon deprotonation) for the synthesis of a series of three luminescent cyclometalated Ir(III) complexes, in which it chelates the metal center with two nitrogen atoms (*i.e.* the pyridine nitrogen and the nitrogen of the azaborine unit). The synthesized complexes have general formula $[Ir(C\hat{}N)_2(\mathbf{FAA})]$, where C^N indicates three different cyclometalating ligands: 2-phenylpyridine in the case of **FAV**; 2-(2,4-difluorophenyl)pyridine in the case of **FAB**; 2-methyl-3-phenylquinoxaline in the case of **FAR**. The synthesis of the three complexes was accomplished starting from reported methods, however the reaction yields are not very high (never above 32 %).

In order to investigate the photophysical properties of all the synthesized compounds, a complete theoretical and experimental characterization was performed. The neutral ligand **FAAH** displays an intense luminescence (PLQY around 25 % in solution). It can be easily protonated on the pyridine nitrogen, and the protonated species $\mathbf{FAAH_2^+}$ is luminescent as well, with a quantum yield in dichloromethane solution which is even grater than that of the neutral **FAAH** (*i.e.* 41 %). In the former case, the emission arises from an excited state whose geometry is not significantly distorted compared to the ground state, as a consequence the emission is almost solvent-independent and displays a well-structured vibronic profile. On the contrary, the emission of $\mathbf{FAAH_2^+}$ arises from a state with a high charge-transfer character (from the borazaronaphthalene unit to the pyridine one), and displays a broad and unstructured emission band around 500 nm. By lowering the temperature up to 77 K it was also possible to record the phosphorescence spectra of both **FAAH** and $\mathbf{FAAH_2^+}$, together with their excited state lifetime.

The photophysical behavior of the three Ir(III) complexes was more difficult to understand, due to a complex interplay between the lowest-energy triplet states,

that were found to be extremely close in energy in all of the three cases. As a consequence, the identification of the emitting states was not straightforward. In the case of **FAV** and **FAB** , experimental evidence and DFT calculations eventually proved that their bright emissions are both centered on the azaborine ligand. As a consequence, the emission wavelength of the two complexes is virtually the same, with only a minor blue shift in the case of the fluorinated one (*i.e.* 490 nm *vs.* 484 nm at 77 K, respectively). The nature of the emitting states was further confirmed by the vibronic progression analysis of their emission spectra recorded at 77 K, which turned out to be somehow comparable to that of the phosphorescence of the free ligand **FAAH** .

On the contrary, **FAR** displays a different emitting state, which is probably ^{3}MLCT/^{3}LLCT in nature. Its emission is centered around 700 nm with a PLQY in solution around 5 %. In this case, a clear identification of the emitting state was not possible since all the three lowest-energy triplets turned out to be virtually isoenergetic. This theoretical evidence is further confirmed by the change in the emitting state observed under different experimental conditions (*i.e.* solution, polymeric, or frozen matrix).

Both the synthesis and the photophysical characterization of the reported compounds were not easy, especially because of the poor chemical stability of the three metal complexes. In particular, complex **FAB** was the less stable compound and, for this reason, it was not possible to fully characterize its photophysics. Further improvements to the present work include better synthesis optimization to increase the reaction yields and more studies to deeper investigate the reasons for the instability of the Iridium complexes.

To conclude, this work demonstrated how properly-functionalized 1,2-azaborines can be used as anionic chelating ligands for Ir(III) complexes. If the stability problems could be overcome, it could also open the way to further studies on complexes containing 2,1-borazaronaphthalene derivatives for optoelectronic applications.

Chapter 4

Experimental Section

4.1 Synthesis

Analytical grade solvents and all the commercially available reagents were used without any further purification, unless otherwise specified. Chromatographic purifications were performed using 230-400 mesh silica gel (pore size 60 Å) and activated basic Al_2O_3 (58 Å, -60 mesh powder).

THF and Et_2O have been dried before use by distillation from Na/benzophenone. Reactions which needed anhydrous conditions were performed under dried nitrogen flow (inert atmosphere). The glassware used in these reactions was placed in an oven at 70 °C for at least 3 hours immediately before use.

^1H, ^{19}F and ^{13}C NMR spectra were recorded on Varian Inova (300 MHz for ^1H and ^{19}F), Varian Mercury (400 MHz for ^1H and ^{19}F) and Varian Inova (600 MHz for ^1H and ^{13}C) spectrometers. All spectra were acquired at 25 °C. Chemical shifts (δ) are reported in ppm relative to the internal standard tetramethylsilane (^1H and ^{13}C) or relative to the residual peak of the solvents (^1H NMR: 7.26 ppm and ^{13}C NMR: 77.0 ppm for $CDCl_3$). ^{13}C NMR spectra were acquired with ^1H broad band decoupled mode. Coupling constants are given in Hz.
The types of carbon atoms were determined by DEPT NMR experiments. The abbreviations used to indicate the multiplicity of signals are: s, singlet; d, doublet; t, triplet; dd, double doublet; ddd, double double doublet; dt, double triplet; m, multiplet. The deuterated solvents for NMR spectra were commercially available.

It was not possible to record the ^{13}C NMR spectra of the Iridium complexes because of their instability in common deuterated solvents over the time required for the acquisition of the spectra.

4.1.1 Synthesis of the azaborine ligand

Synthesis of intermediate 2

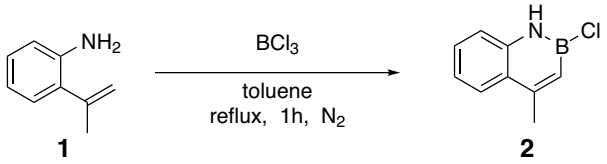

2-isopropenylaniline (476 µl, 3.496 mmol, 1 eq) was dissolved in dry Toluene (50 ml) at 0 °C under nitrogen atmosphere, then 4.5 ml of BCl_3 (1 M hexane solution) were added dropwise (4.545 mmol, 1.3 eq). The yellowish solid formed dissolves to give a pale yellow solution when the mixture is refluxed. After 1 hour the solution was cooled to room temperature and the excess BCl_3 was removed via stripping under vacuum.

Route A: synthesis via Grignard reagent

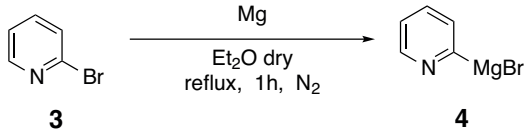

Mg granules (510 mg, 20.980 mmol, 6 eq with respect to aniline **1**) were activated by stirring in a diluted HCl solution (0.1 M in H_2O) for a few minutes and dried in vacuum. Subsequently, they were stirred in dry Et_2O under nitrogen atmosphere overnight. 2-Bromopyridine (500 µl, 5.244 mmol, 1.5 eq) was added dropwise together with a catalytic amount of iodine. The solution was refluxed for 1 hour and then cooled to room temperature to be used in the azaborine synthesis without further purification.

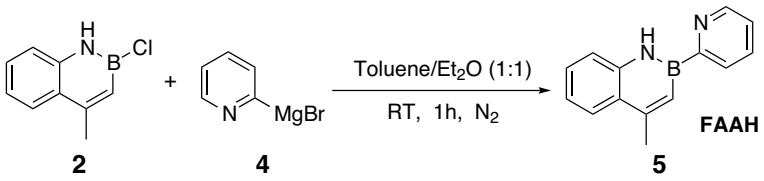

The previously obtained Grignard reagent **4** was added dropwise at room temperature to the solution containing the B-Cl intermediate **2**. After stirring for 1 hour at room temperature, the solvent was removed in vacuum and the resulting crude was purified on silica gel (Hexane:Ethyl acetate = 8:2) to obtain product **5** (**FAAH**) as a yellow-brown solid (75.4 mg, 10% yield). NMR signals confirmed the expected structure (see figures 4.1 and 4.2 on page 54).

^{1}H NMR ($CDCl_3$, 600 MHz) δ 9.40 (s, 1 H), 8.82 (d, J = 4.8 Hz, 1 H), 8.07 (d, J = 7.6 Hz, 1 H), 7.87 (d, J = 8.1 Hz, 1 H), 7.78 (td, J = 7.6 Hz, J = 1.5 Hz 1 H), 7.50-7.46 (m, 2 H), 7.34-7.32 (m, 1 H), 7.25-7.22 (m, 1 H), 7.16 (s, 1 H), 2.70 (d, J = 0.7 Hz, 3 H).

^{13}C NMR ($CDCl_3$, 600 MHz) δ 161.1 (B−C, broaded), 153.0 (C), 149.1 (CH), 140.4 (C), 135.7 (CH), 129.5 (CH), 128.4 (CH), 126.9 (B−CH, broaded), 125.9 (C), 125.6 (CH), 123.9 (CH), 121.0 (CH), 119.3 (CH), 23.2 (CH_3).

Route B: synthesis via 2-Lithiumpyridine

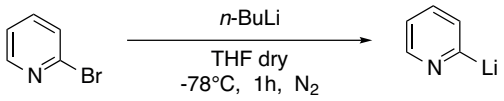

3 **6**

2-Bromopyridine (500 µl, 5.244 mmol, 1.5 eq with respect to aniline **1**) was dissolved in dry THF under nitrogen atmosphere. The solution was then cooled up to −78 °C and *n*-Butyllithium (5.9 ml of a 1.6 M hexane solution, 1.8 eq) was added dropwise to get an orange solution containing 2-Lithiumpyridine **6** that was used for futher azaborine synthesis without any purification.

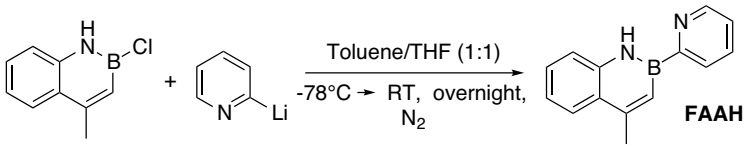

2 **6** **5**

The solution of 2-Lithiumpyridine **6** was added dropwise to the solution containing intermediate **2** at −78 °C, then the mixture was left to reach room temperature and stirred overnight. The solvent was then removed in vacuum and the resulting crude was purified on silica gel (Hexane:Ethyl acetate = 8:2). Product **5** (**FAAH**) was obtained as a yellow-brown solid (52.9 mg, 7% yield). NMR signals confirmed the expected structure.

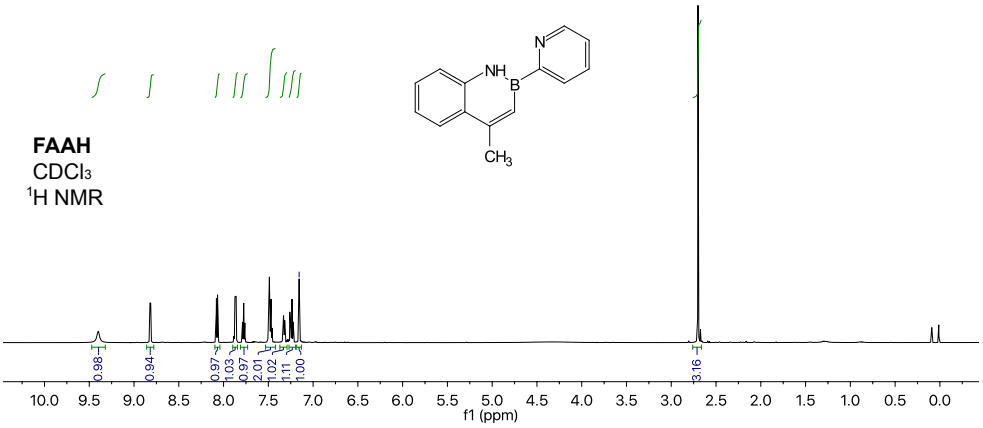

Figure 4.1: 600 MHz ^{1}H NMR spectrum ($CDCl_3$) of **FAAH**

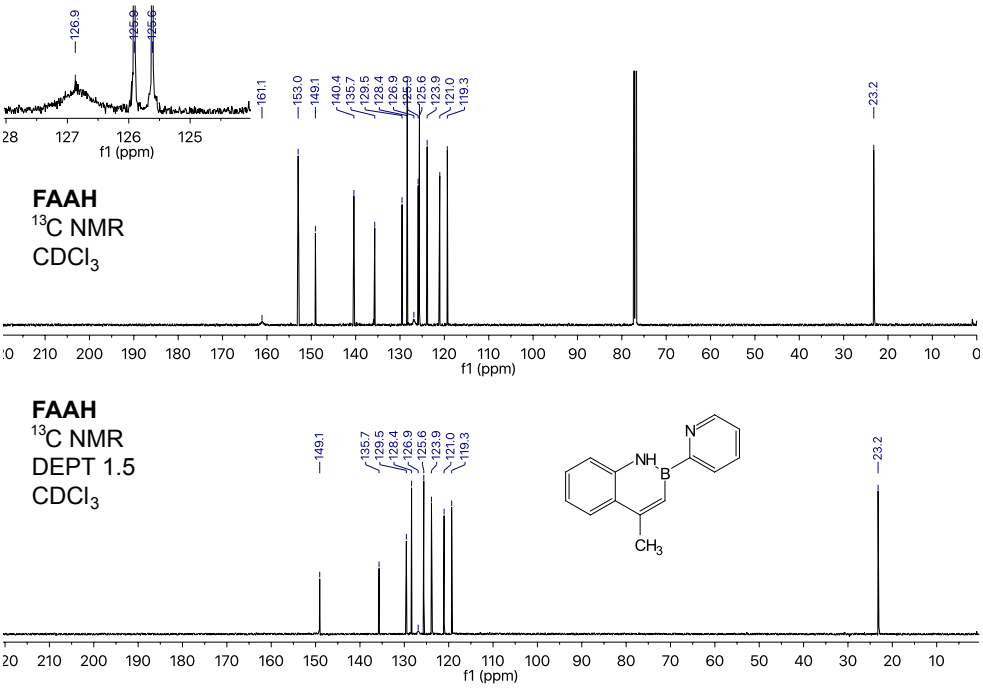

Figure 4.2: 600 MHz ^{13}C NMR spectrum ($CDCl_3$) of **FAAH**

4.1.2 Synthesis of the Ir(III) dimers

General procedure

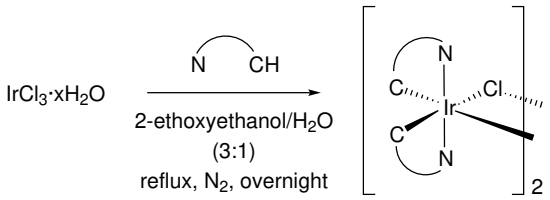

The 3:1 mixture of 2-ethoxyethanol and H_2O (8 ml) was degassed by bubbling N_2 for 15 minutes. $IrCl_3 \cdot nH_2O$ (1 eq) and the desired cyclometalating ligand (2 eq) were then dissolved under nitrogen atmosphere and the solution was refluxed overnight. After cooling to room temperature, some more water was added (≃5 ml) until complete precipitation of the colored solid, which was then filtered on Büchner through a paper filter and washed with both water (2 times x 5 ml) and Hexane (4 times x 5 ml).

Synthesis of dimer 12

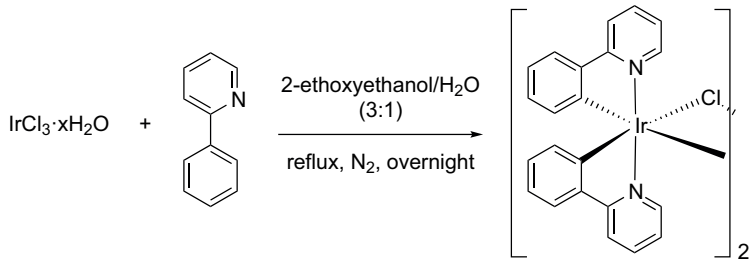

9 **12**

As described in the general procedure $IrCl_3 \cdot nH_2O$ (100.0 mg, 0.335 mmol, 1 eq) was reacted with ppyH **9** (96 µl, 0.670 mmol, 2 eq) to obtain product **12** (129.2 mg, 72% yield). ^1H NMR signals ($CDCl_3$) were in accordance with those found in literature [27].

Synthesis of dimer 13

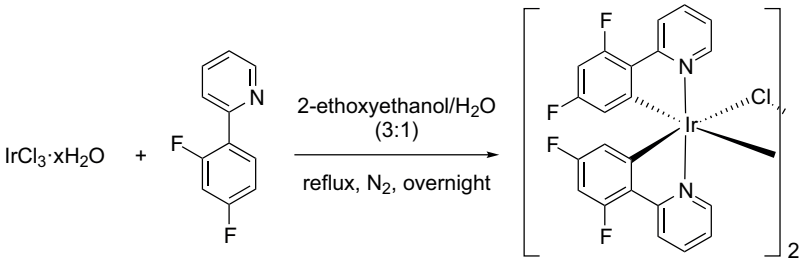

10 **13**

As described in the general procedure $IrCl_3 \cdot nH_2O$ (100.0 mg, 0.335 mmol, 1 eq) was reacted with dfppyH **10** (102 µl, 0.670 mmol, 2 eq) to obtain product **13** (138.2 mg, 68% yield). ^{1}H NMR signals ($CDCl_3$) were in accordance with those found in literature [28].

Synthesis of dimer 14

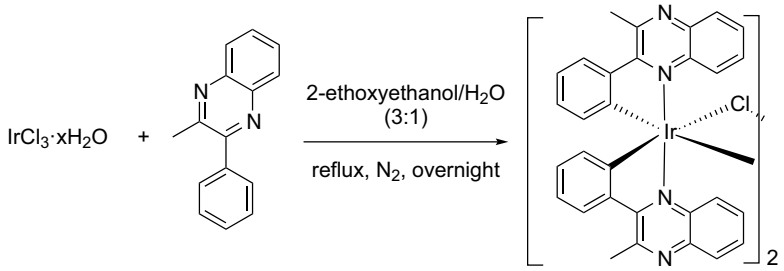

11 **14**

As described in the general procedure $IrCl_3 \cdot nH_2O$ (100.0 mg, 0.335 mmol, 1 eq) was reacted with pquH **11** (147.6 mg, 0.670 mmol, 2 eq) to obtain product **14** (149.0 mg, 67% yield). ^{1}H NMR signals were congruent with the expected ones.

^{1}H NMR ($CDCl_3$, 400 MHz) δ 8.15 (d, J = 8.9 Hz, 4 H), 7.95 (d, J = 7.8 Hz, 4 H), 7.68 (dd, J = 8.4 Hz, J = 0.9 Hz, 4 H), 7.56 (t, J = 7.2 Hz, 4 H), 6.93-6.78 (m, 8 H), 6.31 (t, J = 7.6 Hz, 4 H), 5.75 (d, J = 7.8 Hz, 4 H), 3.18 (s, 12 H).

4.1.3 Synthesis of the Ir(III)-azaborine complexes

General procedure

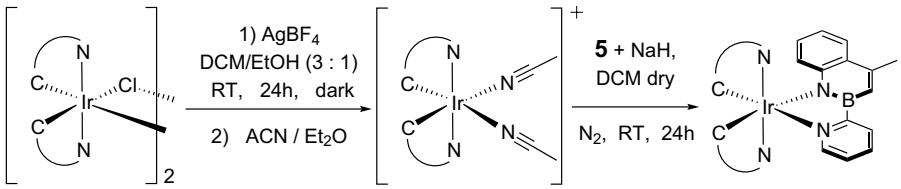

The desired Ir(III) dimeric complex (1 eq) was dissolved in a 3:1 mixture of DCM/EtOH (8 ml), then $AgBF_4$ (2 eq) was added in the absence of light. The mixture was kept in the dark and stirred at room temperature for 24 hours, then it was filtered through a PTFE filter to remove AgCl. The solution was eventually evaporated to dryness and the resulting solid was dissolved in acetonitrile and precipitated twice with Et_2O.
The obtained Ir(III) solvato complexes were used in the next step of the synthesis without further purification.

Azaborine **5** (2.2 eq) was dissolved in dry DCM (6 ml) under nitrogen atmosphere. NaH was then added (2.4 eq with respect to azaborine **5**) and the mixture was stirred for 2 hours at room temperature.

In the last step the Ir(III) solvato complex was dissolved in dry DCM (4 ml) under nitrogen atmosphere and the solution containing the base-treated azaborine **5** (**FAAH**) was added dropwise. The mixture was stirred at room temperature for 24 hours, after which the resulting crude was purified on Al_2O_3.

Synthesis of complex 15 (FAV)

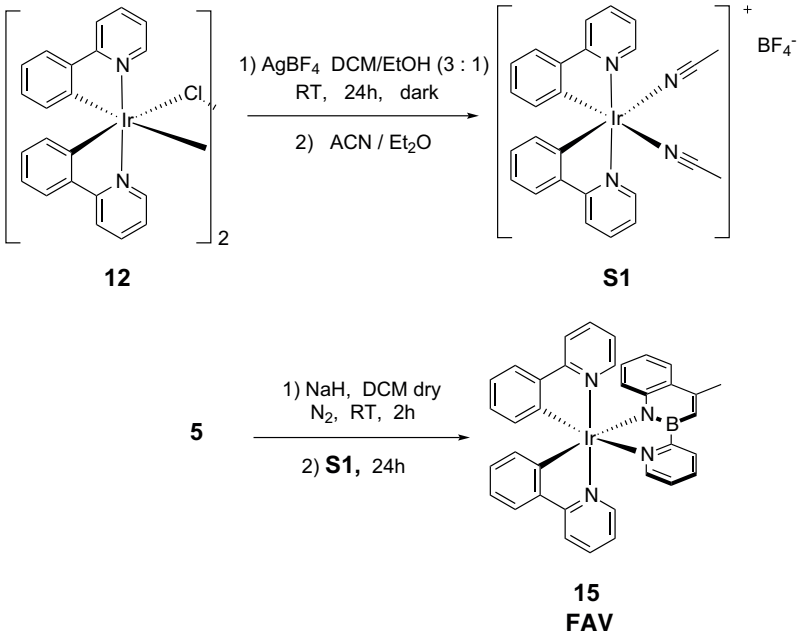

Following the general procedure the dimeric complex **12** (20.0 mg, 0.019 mmol, 1 eq) was treated with $AgBF_4$ (7.3 mg, 0.037 mmol, 2 eq) and the acetonitrile solvato complex **S1** was obtained as a white solid. **FAAH (5)** (9.1 mg, 0.041 mmol, 2.2 eq) was pre-treated with NaH (4.0 mg of a 60 % dispersion in mineral oil, 0.098 mmol, 2.4 eq with respect to azaborine **5**) and added to a DCM solution of **S1**.

The resulting crude was purified on Al_2O_3 (Hexane:Ethyl acetate = 7:3) and complex **FAV (15)** was obtained as a yellow solid (8.6 mg, 32% yield). NMR signals were in accordance with the expected structure (see figure 4.3 on page 61).

^{1}H NMR ($CDCl_3$, 300 MHz) δ 8.32 (ddd, J = 5.8 Hz, J = 1.5 Hz, J = 0.6 Hz, 1 H), 8.18 (ddd, J = 7.6 Hz, J = 1.6 Hz, J = 0.9 Hz, 1 H), 7.81 (d, J = 7.8 Hz, 1 H), 7.73-7.68 (m, 3 H), 7.65-7.44 (m, 7 H), 7.10 (d, J = 0.8 Hz, 1 H), 6.96-6.68 (m, 9 H), 6.43-6.40 (m, 1 H), 6.21 (dd, J = 7.6 Hz, J = 1.0 Hz, 1 H), 2.71 (d, J = 0.8 Hz, 3 H).

Synthesis of complex 16 (FAB)

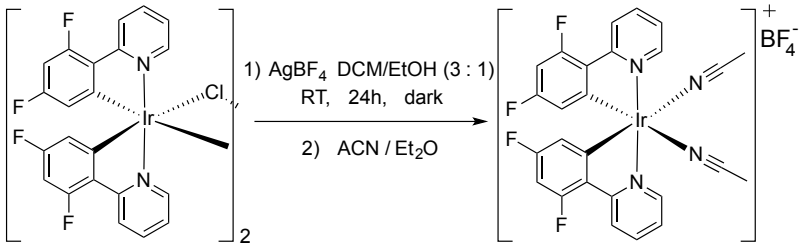

13 **S2**

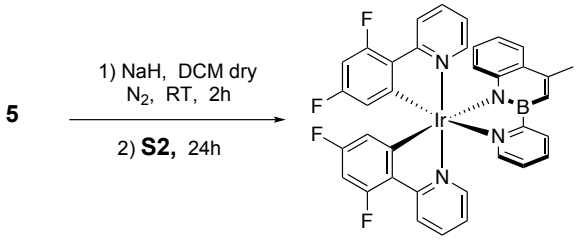

16
FAB

Following the general procedure the dimeric complex **13** (35.1 mg, 0.029 mmol, 1 eq) was treated with $AgBF_4$ (11.3 mg, 0.058 mmol, 2 eq) and the acetonitrile solvato complex **S2** was obtained as a pale yellow solid.
Azaborine **5** (14.0 mg, 0.064 mmol, 2.2 eq) was pre-treated with NaH (6.1 mg of a 60 % dispersion in mineral oil, 0.153 mmol, 2.4 eq with respect to azaborine **5**) and added to a DCM solution of **S2**. The resulting crude was purified on Al_2O_3 (Hexane:Ethyl acetate = 8:2) and complex **FAB** (**16**) was obtained as a yellow solid (11.5 mg, 25% yield). NMR signals were in accordance with the expected structure (see figure 4.4 on page 62 for the ^{1}H NMR spectrum).

^{1}H NMR ($CDCl_3$, 400 MHz) δ 8.31 (ddd, J = 5.9 Hz, J = 1.7 Hz, J = 0.8 Hz, 1 H), 8.25-8.19 (m, 2 H), 8.15 (d, J = 8.6 Hz, 1 H), 7.74 (dd, J = 8.1 Hz, J = 1.7 Hz, 1 H), 7.70-7.61 (m, 3 H), 7.56-7.52 (m, 1 H), 7.48 (ddd, J = 5.9 Hz, J = 1.6 Hz, J = 0.8 Hz, 1 H), 7.36 (dd, J = 8.8 Hz, J = 1.1 Hz, 1 H), 7.08 (d, J = 0.8 Hz, 1 H), 6.99 (ddd, J = 7.3 Hz, J = 5.7 Hz, J = 1.6 Hz, 1 H), 6.93 (ddd, J = 8.1 Hz, J = 6.8 Hz, J = 1.3 Hz, 1 H), 6.84-6.80 (m, 2 H), 6.76 (ddd, J = 7.4 Hz, J = 6.0 Hz, J = 1.4 Hz, 1 H), 6.49-6.38 (m, 2 H), 5.81 (dd, J = 8.9 Hz, J = 2.3 Hz, 1 H), 5.64 (dd, J = 8.4 Hz, J = 2.4 Hz, 1 H), 2.70 (d, J = 0.9 Hz, 3 H).

^{19}F NMR ($CDCl_3$, 400 MHz) δ -107.43 (dd, J = 18.8 Hz, 9.3 Hz, 1 F) -108,74 (dd, J = 19.1 Hz, 9.3 Hz, 1 F) -110.05 (t, J = 11.6 Hz, 1 F) -110.65 (t, J = 12.3 Hz, 1 F).

Synthesis of complex 17 (FAR)

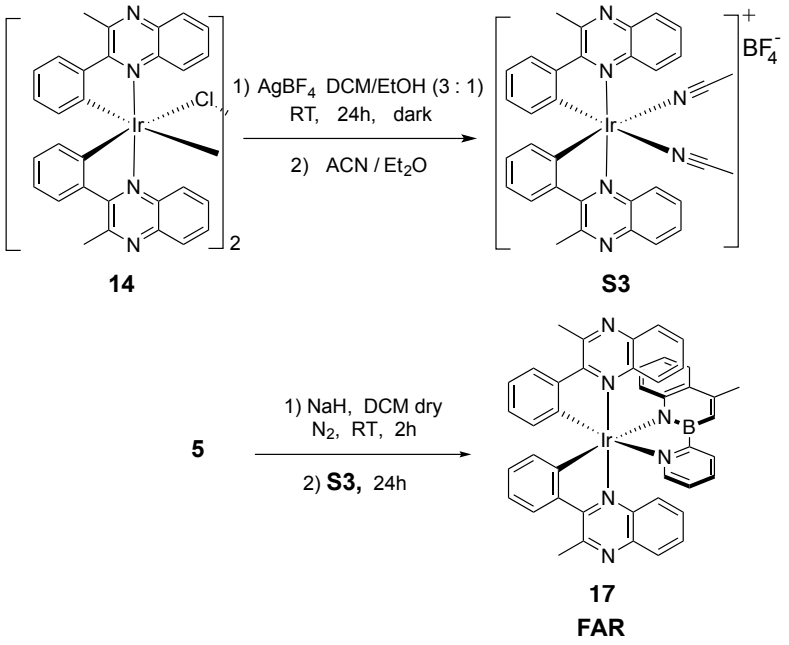

Following the general procedure the dimeric complex **14** (38.4 mg, 0.029 mmol, 1 eq) was treated with $AgBF_4$ (11.3 mg, 0.058 mmol, 2 eq) and the acetonitrile solvato complex **S3** was obtained as a red-brown solid.
Azaborine **5** (14.0 mg, 0.064 mmol, 2.2 eq) was pre-treated with NaH (6.1 mg of a 60 % dispersion in mineral oil, 0.153 mmol, 2.4 eq with respect to azaborine **5**) and added to a DCM solution of **S3**.

The resulting crude was purified on Al_2O_3 (Hexane:Ethyl acetate = 6:4) and complex **FAR** (**17**) was obtained as a dark red solid (5.3 mg, 11% yield). NMR signals were in accordance with the expected structure (see figure 4.5 on page 62).

^{1}H NMR ($CDCl_3$, 300 MHz) δ 9.32 (dd, J = 9.0 Hz, J = 1.0 Hz, 1 H), 8.36 (dd, J = 8.2 Hz, J = 0.9 Hz, 1 H), 7.89 (dd, J = 8.2 Hz, J = 1.4 Hz, 1 H), 7.82 (dd, J = 8.2 Hz, J = 0.8 Hz, 1 H), 7.75-7.71 (m, 1 H), 7.69 (ddd, J = 4.4 Hz, J = 1.4 Hz, J = 0.8 Hz, 1 H), 7.66-7-63 (m, 1 H), 7.50 (td, J = 7.6 Hz, J = 1.5 Hz, 1 H), 7,41 (ddd, J = 8.2 Hz, J = 6.9 Hz, J = 1.2 Hz, 1 H), 7.35 (ddd, J = 8.2 Hz, J = 6.9 Hz, J = 1.3 Hz, 1 H), 7.10 (ddd, J = 8.3 Hz, J = 7.1 Hz, J = 1.4 Hz, 1 H), 7-05-7.02 (m, 1 H), 6.98-6.79 (m, 5 H), 6.76-6.69 (m, 4 H), 6.65-5.58 (m, 2 H), 6.40 (dd, J = 7.7 Hz, J = 0.9 Hz, 1 H), 6.36 (d, J = 0.9 Hz, 1 H), 3.36 (s, 3 H), 2.62 (s, 3 H), 2.49 (d, J = 0.9 Hz, 3 H).

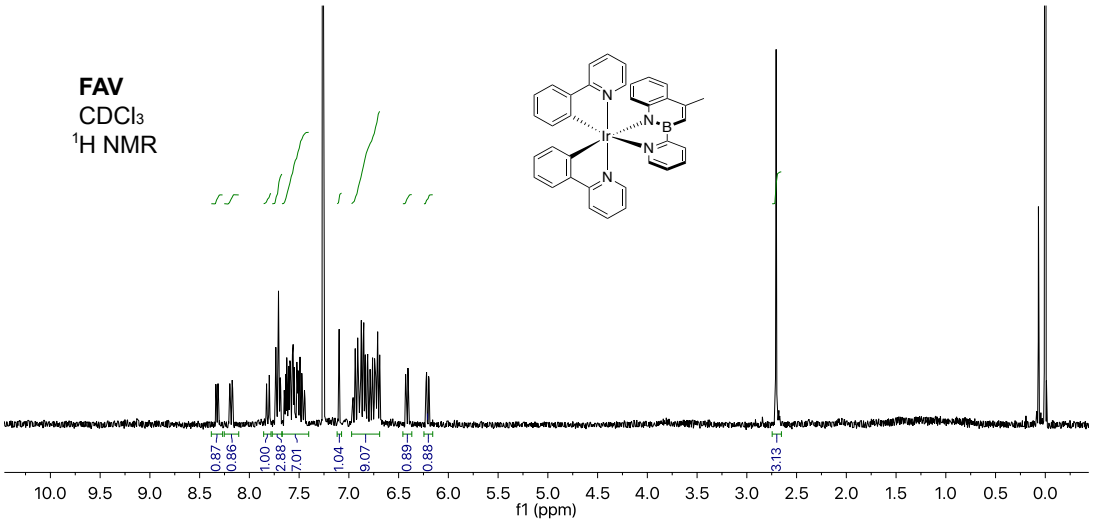

Figure 4.3: 300 MHz ^{1}H NMR spectrum ($CDCl_3$) of **FAV** (complex **15**)

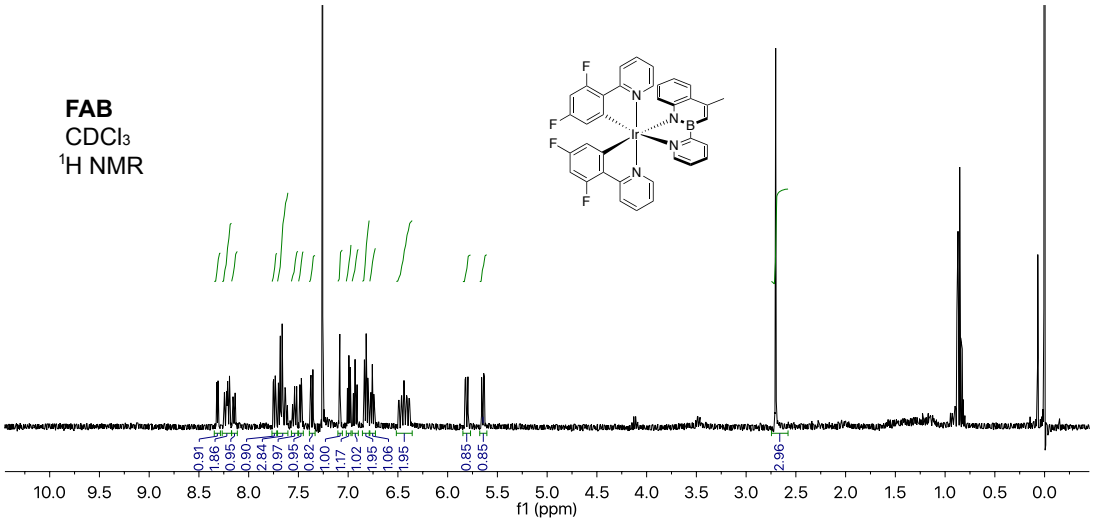

Figure 4.4: 400 MHz ^{1}H NMR spectrum ($CDCl_3$) of **FAB** (complex **16**)

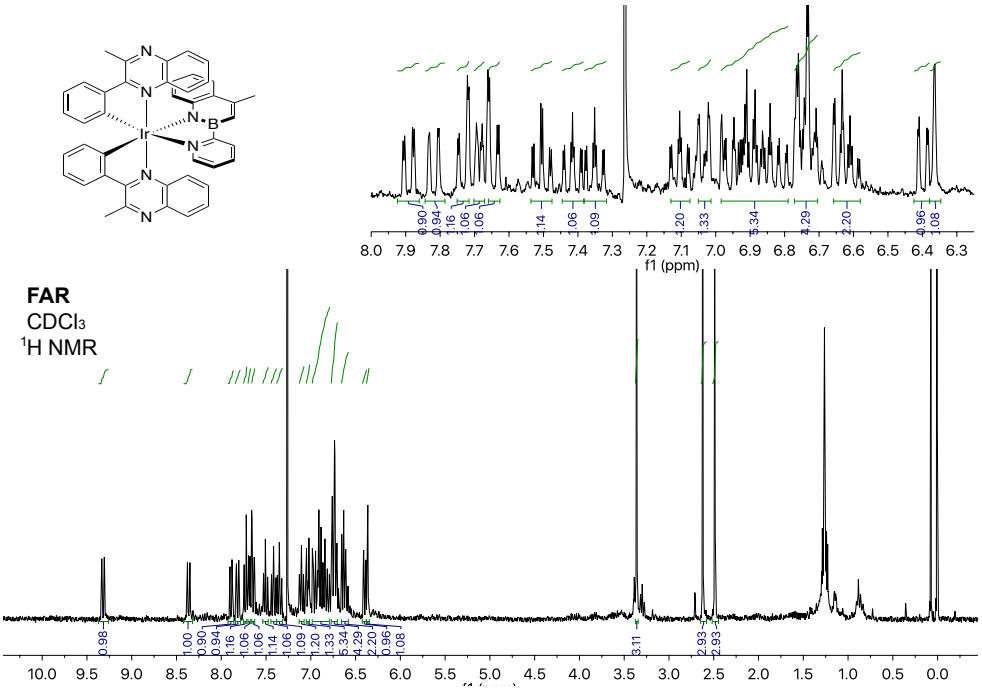

Figure 4.5: 300 MHz ^{1}H NMR spectrum ($CDCl_3$) of **FAR** (complex **17**)

4.2 Photophysical characterization

4.2.1 Absorption and emission spectroscopy

All absorption and emission measurements in solution were carried out in spectroscopic grade solvents (*i.e.* acetonitrile and dichloromethane) used without further purification. In both cases Suprasil quartz cuvettes, having 1 cm path length, were used.

In the case of solid-state measurements, poly(methyl-methacrylate) (PMMA) films doped with 1 % w/w of the samples were prepared by drop casting from dichloromethane solution on a Suprasil quartz slide (1 × 1 in). The thickness of the films was not accurately controlled, but it is within the 100 µm to 500 µm range.

Absorption spectra in solution were recorded with a Perkin-Elmer Lambda 950 spectrophotometer making a double baseline (*i.e.* both at 100% and 0% of transmittance).

All the emission spectra (both in solid state and solution) were recorded using an Edinburgh FLSP90 spectrometer equipped with a Peltier-cooled Hamamatsu R928 photomultiplyer tube (sensitive in the 185 nm to 850 nm range) or a Hamamatsu R5509-72 Supercooled photomultiplyer tube (sensitive in the 600 nm to 1700 nm range). To record the emission spectra of the Iridium complexes in solution, the samples were deoxygenated by bubbling Argon for 30 min. The concentration of the samples was adjusted to obtain absorption values <0.2 at the excitation wavelength. An Edinburgh Xe900 450 W Xenon arc lamp was used as the excitation source. All the reported spectra are corrected for the instrumental response using a calibration curve.

To record the 77 K luminescence spectra, the samples were put in quartz tubes (2 mm inner diameter) and inserted in a special quartz Dewar flask filled with liquid nitrogen. Butyronitrile was used as solvent in order to obtain a transparent glass.

4.2.2 Determination of photoluminescence quantum yields

The deactivation of excited states includes both radiative and non-radiative processes, each one having its own kinetic constant. The photoluminescence quantum yield (PLQY or Φ_{em}) is a parameter that quantifies the relevance of radiative pathways (*i.e.* emission of light) over non-radiative ones. The PLQY can be calculated as the ratio of the radiative constant k_r to the sum of the kinetic constants of all the deactivation processes:

$$\Phi_{em} = \frac{\text{number of emitted photons}}{\text{number of absorbed photons}} = \frac{k_r}{k_r + k_{nr}} \tag{4.1}$$

k_{nr} being the kinetic constant for non radiative deactivation.

Photoluminescence quantum yields in solution

The quantum yields in solution were determined in a relative way by comparison with suitable standards with known quantum yields. The emission spectra of both the sample and the standard were recorded under the same experimental conditions (excitation wavelength, excitation and emission slits). Knowing the integral of the recorded emission spectra, the PLQY can be calculated using the formula:

$$\Phi_{samp} = \Phi_{ref} \times \frac{A_{ref}}{A_{samp}} \times \frac{n_{samp}^2}{n_{ref}^2} \times \frac{I_{sample}}{I_{ref}} \tag{4.2}$$

where:

Φ = photoluminescence quantum yield;

A = absorbance at the excitation wavelength;

n = refractive index of the solvent;

I = integral of the emission spectrum (subtended area).

The subscripts refer to the sample ("samp") or to the standard ("ref"). The previous formula is valid only for diluted solution whose absorbance at the excitation wavelength is lower than 0.2. Two different standards were used:

- air-equilibrated solution of quinine sulfate in 0.1 N H_2SO_4 (Φ = 54.6 %) [37];
- air-equilibrated $[Ru(bpy)_3][Cl]_2$ water solution (Φ = 2.8 %) [37].

Solid-state photoluminescence quantum yields

Solid-state PLQY values were determined with an absolute method. The Edinburgh FLSP90 spectrometer was equipped with a barium sulfate-coated integrating sphere (3 inches diameter) and PLQYs were determined following the procedure described by Wurth *et al.* [38]. The integrating sphere detects all light absorbed and emitted by the excited sample, and hence allows for the absolute measurement of the fluorescence quantum yield by simply comparing the number of emitted photons with the number of absorbed photons.

Two spectra are recorded under the same experimental conditions with an emission range that covers both the excitation region and the sample emission. One spectrum is acquired with the solid sample inside the sphere, the other one placing a blank at the sample position. Comparing the two spectra it is possible to calculate the number of absorbed photons from the decrease in the incident excitation light intensity (caused by the absorbing sample in the integrating sphere),

while the number of emitted photons is given by the area subtended by the emission band of the sample. Experimental uncertainty for PLQYs determined with this method is estimated to be ± 10 %.

4.2.3 Excited-state lifetimes

The deactivation processes of an excited-state molecule can generally be described with a first-order kinetics:

$$-\frac{d[A^*]}{dt} = (k_r + k_{nr}) \cdot [A^*] \tag{4.3}$$

where

$[A^*]$ = concentration of excited-state molecules;

k_r = emission kinetic constant (radiative deactivation);

k_{nr} = kinetic constant of the non-radiative processes.

Solving the above equation:

$$\frac{[A^*]}{[A^*]_0} = e^{-(k_r+k_{nr})\,t} \tag{4.4}$$

The excited-state lifetime (τ) is defined as the time required to reduce the population of the excited-state by a factor of $1/e$, hence:

$$\frac{[A^*]}{[A^*]_0} = e^{-(k_r+k_{nr})\,t} = e^{-1} \tag{4.5}$$

$$\tau = \frac{1}{k_r + k_{nr}} \tag{4.6}$$

τ can therefore be calculated as the inverse of the sum of the kinetic constants of all the deactivation processes.

A simple way to determine τ is to monitor the time evolution of the emission intensity, assuming it to be proportional to the number of excited-state molecules at every given time.

Such method was used to determine the excited-state phosphorescence lifetime of the azaborine ligand at 77 K, using the Edinburgh FLSP90 spectrometer and the above-mentioned Xe lamp as excitation source. Throughout the measurement the sample was continuously excited for 10 s, then the excitation source (controlled by the excitation shutter) was turned off in order to study the decay kinetics. The emission signal was recorded for a minute, while keeping a fixed excitation and a fixed emission wavelength. The decay of the emission intensity

over time was then fitted using a mono-exponential decay function to determine the excited-state lifetime.

Even if the measurement from a single excitation-emission cycle is in principle the simplest way to obtain the decay profile of the signal, the above-described method is applicable only for long lifetimes (*i.e.* few seconds to minutes) which allow the recording of the emission intensity over time after the excitation has been turned off. In all the other cases the excited-state lifetimes both in solution and in the solid-state were determined using the Time-Correlated Single Photon Counting technique (TCSPC) using a HORIBA Jobin Yvon IBH FluoroHub controlling a spectrometer equipped with a red-sensitive Hamamatsu R-3237-01 detector (185 nm to 850 nm) and two different kinds of pulsed sources: (i) NanoLEDs (λ_{exc} = 331 nm, 465 nm) for emission lifetimes in the nanosecond - few milliseconds timescale, (ii) SpectraLEDs (λ_{exc} = 464 nm) for longer decays.

The TCSPC technique is based on the repetitive, precisely timed registration of single photons emitted by a luminescent sample. The reference for the timing is the corresponding excitation pulse. The time is measured between the excitation pulse and the observed photon and stored in a histogram (see Figure 4.6). The x-axis is the time difference and the y-axis the number of photons detected for this time difference. The time difference between excitation and emission is measured by electronics that act like a stopwatch. Provided that the probability of detecting any emitted photon is low (typically 1 photon per 100 excitation pulses), the histogram of photon arrivals per time bin represents the time decay that would result from a "single shot" time-resolved recording. If the count rate is higher, the histogram is biased to shorter times. This is because, following the excitation pulse, more photons are emitted at early times than at late times. If all these photons could be measured, then the histogram of arrival times would represent the intensity decay. However, if many arrive, and only the first is counted, then the intensity decay is distorted to shorter times. [39, 40].

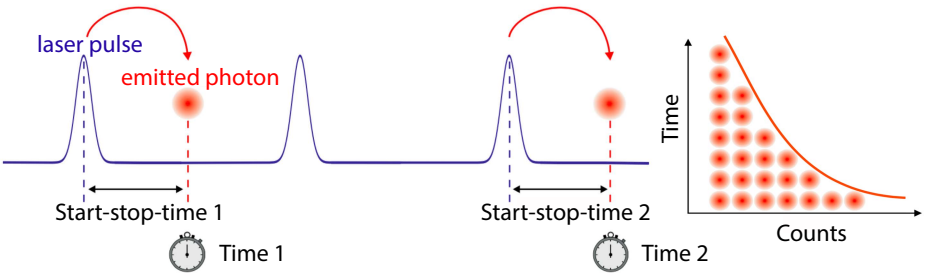

Figure 4.6: Measurement of start-stop times in time-resolved fluorescence measurement with TCSPC and relative histogram [40].

The overall timing precision of the TCSPC system is its Instrument Response Function (IRF). An ideal system (*i.e* infinitely sharp excitation pulse and infinitely accurate detectors and electronics) should have an infinitely narrow IRF. Any deviation from this ideal situation results in a broadening of the IRF. The measured fluorescence decay is actually the convolution of the "true" physical process of exponential decay with the IRF. To extract the parameters of the "true" decay process from the collected histograms the IRF should be measured as well in order to perform a deconvolution. The typical approach to record the IRF is to place a scattering medium in the sample compartment so that there is no fluorescence but only some scattered excitation light reaching the detector [40].

The analysis of the luminescence decay profiles *vs* time was accomplished with the DAS6 Decay Analysis Software provided by the manufacturer, and the quality of the fit was assessed with the χ^2 value close to unity and with the residuals regularly distributed along the time axis. Experimental uncertainty for τ determination is estimated to be ± 5 %.

4.3 Computational details

Density Functional Theory (DFT) calculations were carried out using the D.01 revision of the Gaussian 09 program package [41] in combination with the M06 global-hybrid meta-GGA exchange-correlation functional [42, 43]. The fully relativistic Stuttgart/Cologne energy-consistent pseudopotential with multi-electron fit was used to replace the first 60 inner-core electrons of the Iridium metal center (*i.e.* ECP60MDF) [44] and was combined with the triple-ζ basis set (*i.e.* cc-pVTZ-PP basis) [44]. For all the other atoms the Pople 6-31G(d,p) was adopted [45]. All the investigated compounds were fully optimized both in their singlet ground state S_0 and in their lowest triplet state T_1 without symmetry constraint, by using the polarizable continuum model (PCM) to simulate the acetonitrile solvation effects [46–48].

Frequency calculations were always used to confirm that the found stationary point was a minimum on the corresponding potential energy surface (*i.e.* no imaginary frequencies).

Time-dependent DFT calculations (TD-DFT) [49–51] carried out at the same level of theory used for geometry optimizations, were used to simulate the absorption spectrum of the free ligand **FAAH** and the protonated $\mathbf{FAAH_2^+}$, taking into account the first 5 excited singlets. In this context, S_1 was also optimized to simulate the emission spectrum. The theoretical absorption spectrum of **FAAH** was also calculated taking into account dynamic effects, following a described procedure to compute vibrationally-resolved electronic spectra using Gaussian [32].

TD-DFT calculations were also used to simulate the electronic absorption

spectra of the investigated Iridium complexes in their optimized S_0 geometry. The first 100 excited singlets and 25 triplet vertical excitations were computed for all the complexes. In the case of the three Iridium complexes, the three lowest triplet states T_1, T_2 and T_3 were optimized by means of TD-DFT calculations taking into account the first 9 excited triplets. Natural transition orbitals (NTOs) transformations were adopted to obtain a clear and compact orbital representation for the electronic transition density matrix in the case of complex multiconfigurational excitations [34].

To investigate the nature of the triplet states, geometry optimizations and frequency calculations were performed at the spin unrestricted UM06 level of theory, imposing a spin multiplicity of 3. The emission energy from the lowest triplet excited state was estimated as adiabatic energy difference (*i.e.* the difference between the SCF energies of T_1 and S_1 in their minimum conformation).

All the pictures showing molecular orbitals and spin-density surfaces were created using GaussView 5 [52].

Bibliography

(1) P. G. Campbell, A. J. V. Marwitz and S.-Y. Liu, *Angew. Chem. Int. Ed.*, 2012, **51**, 6074–6092.

(2) A. Stock and E. Pohland, *Berichte der deutschen chemischen Gesellschaft (A and B Series)*, 1926, **59**, 2215–2223.

(3) S. R. Wisniewski, C. L. Guenther, O. A. Argintaru and G. A. Molander, *J. Org. Chem.*, 2014, **79**, 365–378.

(4) A. Mazzanti, E. Mercanti and M. Mancinelli, *Org. Lett.*, 2016, **18**, 2692–2695.

(5) A. N. Brown, L. N. Zakharov, T. Mikulas, D. A. Dixon and S.-Y. Liu, *Org. Lett.*, 2014, **16**, 3340–3343.

(6) T. Agou, J. Kobayashi and T. Kawashima, *Org. Lett.*, 2006, **8**, 2241–2244.

(7) M. J. S. Dewar, V. P. Kubba and R. Pettit, *J. Chem. Soc.*, 1958, 3073–3076.

(8) M. J. S. Dewar, V. P. Kubba and R. Pettit, *J. Chem. Soc.*, 1958, 3076–3079.

(9) M. J. S. Dewar and R. Dietz, *J. Chem. Soc.*, 1959, 2728–2730.

(10) G. H. M. Davies, Z.-Z. Zhou, M. Jouffroy and G. A. Molander, *J. Org. Chem.*, 2017, **82**, 549–555.

(11) R. Kwong, B. Ma, J. Tsai, S. Beers, E. Barron, G. Kottas and A. Dyatkin, *pat.*, US8586203 B2, US Patent App. 12/781,493, 2010.

(12) H. Xu, R. Chen, Q. Sun, W. Lai, Q. Su, W. Huang and X. Liu, *Chem. Soc. Rev.*, 2014, **43**, 3259–3302.

(13) R. H. Friend, R. W. Gymer, A. B. Holmes, J. H. Burroughes, R. N. Marks, C. Taliani, D. D. C. Bradley, D. A. D. Santos, J. L. Bredas, M. Logdlund and W. R. Salaneck, *Nature*, 1999, **397**, 121–128.

(14) V. V. Grushin, N. Herron, D. D. LeCloux, W. J. Marshall, V. A. Petrov and Y. Wang, *Chem. Commun.*, 2001, 1494–1495.

(15) K. Dedeian, P. I. Djurovich, F. O. Garces, G. Carlson and R. J. Watts, *Inorg. Chem.*, 1991, **30**, 1685–1687.

(16) M. Nonoyama, *Bull. Chem. Soc. Jpn.*, 1974, **47**, 767–768.

(17) L. Flamigni, A. Barbieri, C. Sabatini, B. Ventura and F. Barigelletti, in *Photochemistry and Photophysics of Coordination Compounds II*, ed. V. Balzani and S. Campagna, Springer Berlin Heidelberg, Berlin, Heidelberg, 2007, pp. 143–203.

(18) B. Schmid, F. O. Garces and R. J. Watts, *Inorg. Chem.*, 1994, **33**, 9–14.

(19) R. Englman and J. Jortner, *Mol. Phys.*, 1970, **18**, 145–164.

(20) K. M. Davies, M. J. S. Dewar and P. Rona, *Journal of the American Chemical Society*, 1967, **89**, 6294–6297.

(21) Q. I. Churches, J. F. Hooper and C. A. Hutton, *J. Org. Chem.*, 2015, **80**, 5428–5435.

(22) S. Lamansky, P. Djurovich, D. Murphy, F. Abdel-Razzaq, H.-E. Lee, C. Adachi, P. E. Burrows, S. R. Forrest and M. E. Thompson, *J. Am. Chem. Soc.*, 2001, **123**, 4304–4312.

(23) F. Monti, A. Baschieri, E. Matteucci, A. Mazzanti, L. Sambri, A. Barbieri and N. Armaroli, *Faraday Discuss.*, 2015, **185**, 233–248.

(24) D. Schneidenbach, S. Ammermann, M. Debeaux, A. Freund, M. Zöllner, C. Daniliuc, P. G. Jones, W. Kowalsky and H.-H. Johannes, *Inorg. Chem.*, 2010, **49**, 397–406.

(25) A. J. Canty and G. van Koten, *Acc. Chem. Res.*, 1995, **28**, 406–413.

(26) M. I. Bruce, *Angew. Chem. Int. Ed.*, 1977, **16**, 73–86.

(27) A. A. Rachford, R. Ziessel, T. Bura, P. Retailleau and F. N. Castellano, *Inorg. Chem.*, 2010, **49**, 3730–3736.

(28) E. Baranoff, B. F. E. Curchod, F. Monti, F. Steimer, G. Accorsi, I. Tavernelli, U. Rothlisberger, R. Scopelliti, M. Grätzel and M. K. Nazeeruddin, *Inorg. Chem.*, 2012, **51**, 799–811.

(29) A. B. Tamayo, B. D. Alleyne, P. I. Djurovich, S. Lamansky, I. Tsyba, N. N. Ho, R. Bau and M. E. Thompson, *J. Am. Chem. Soc.*, 2003, **125**, 7377–7387.

(30) A. Baschieri, F. Monti, E. Matteucci, A. Mazzanti, A. Barbieri, N. Armaroli and L. Sambri, *Inorg. Chem.*, 2016, **55**, 7912–7919.

(31) F. Monti, A. Baschieri, I. Gualandi, J. J. Serrano-Pérez, J. M. Junquera-Hernández, D. Tonelli, A. Mazzanti, S. Muzzioli, S. Stagni, C. Roldan-Carmona, A. Pertegás, H. J. Bolink, E. Ortí, L. Sambri and N. Armaroli, *Inorg. Chem.*, 2014, **53**, 7709–7721.

(32) M. B. V. Barone, J. Bloino, *Vibrationally-resolved electronic spectra in GAUSSIAN 09*, tech. rep., Scuola Normale Superiore, Piazza dei Cavalieri, 7 I-56126 Pisa, Italy, 2009.

(33) M. de Jong, L. Seijo, A. Meijerink and F. T. Rabouw, *Phys. Chem. Chem. Phys.*, 2015, **17**, 16959–16969.

(34) R. L. Martin, *The Journal of Chemical Physics*, 2003, **118**, 4775–4777.

(35) A. J. Lees, *Comments on Inorganic Chemistry*, 1995, **17**, 319–346.

(36) J. V. Caspar and T. J. Meyer, *Inorganic Chemistry*, 1983, **22**, 2444–2453.

(37) A. Juris, L. Moggi and M. Gandolfi, *Manuale del fotochimico. Tecniche e metodologie*, Bononia University Press, 2006.

(38) C. Würth, M. Grabolle, J. Pauli, M. Spieles and U. Resch-Genger, *Nat. Protocols*, 2013, **8**, 1535–1550.

(39) J. Lakowicz, *Principles of Fluorescence Spectroscopy*, Kluwer Academic/Plenum, 1999.

(40) M. Wahl, *Time-Correlated Single Photon Counting*, tech. rep., PicoQuant GmbH, Rudower Chaussee 29, 12489 Berlin (Germany), 2014.

(41) M. J. Frisch, G. W. Trucks, H. B. Schlegel, G. E. Scuseria, M. A. Robb, J. R. Cheeseman, G. Scalmani, V. Barone, B. Mennucci, G. A. Petersson, H. Nakatsuji, M. Caricato, X. Li, H. P. Hratchian, A. F. Izmaylov, J. Bloino, G. Zheng, J. L. Sonnenberg, M. Hada, M. Ehara, K. Toyota, R. Fukuda, J. Hasegawa, M. Ishida, T. Nakajima, Y. Honda, O. Kitao, H. Nakai, T. Vreven, J. A. Montgomery, J. E. Peralta, F. Ogliaro, M. Bearpark, J. J. Heyd, E. Brothers, K. N. Kudin, V. N. Staroverov, R. Kobayashi, J. Normand, K. Raghavachari, A. Rendell, J. C. Burant, S. S. Iyengar, J. Tomasi, M. Cossi, N. Rega, J. M. Millam, M. Klene, J. E. Knox, J. B. Cross, V. Bakken, C. Adamo, J. Jaramillo, R. Gomperts, R. E. Stratmann, O. Yazyev, A. J. Austin, R. Cammi, C. Pomelli, J. W. Ochterski, R. L. Martin, K. Morokuma, V. G. Zakrzewski, G. A. Voth, P. Salvador, J. J. Dannenberg, S. Dapprich, A. D. Daniels, Farkas, J. B. Foresman, J. V. Ortiz, J. Cioslowski and D. J. Fox, *Gaussian 09, Revision D.01*, Wallingford CT, 2009.

(42) Y. Zhao and D. G. Truhlar, *Theoretical Chemistry Accounts*, 2008, **120**, 215–241.

(43) Y. Zhao and D. G. Truhlar, *Accounts of Chemical Research*, 2008, **41**, 157–167.

(44) D. Figgen, K. A. Peterson, M. Dolg and H. Stoll, *The Journal of Chemical Physics*, 2009, **130**, 164108.

(45) M. M. Francl, W. J. Pietro, W. J. Hehre, J. S. Binkley, M. S. Gordon, D. J. DeFrees and J. A. Pople, *The Journal of Chemical Physics*, 1982, **77**, 3654–3665.

(46) O. Tapia and J. Bertràn, *Solvent Effects and Chemical Reactivity*, Springer, 2003.

(47) J. Tomasi and M. Persico, *Chemical Reviews*, 1994, **94**, 2027–2094.

(48) J. Tomasi, B. Mennucci and R. Cammi, *Chemical Reviews*, 2005, **105**, 2999–3094.

(49) R. Bauernschmitt and R. Ahlrichs, *Chemical Physics Letters*, 1996, **256**, 454 –464.

(50) R. E. Stratmann, G. E. Scuseria and M. J. Frisch, *The Journal of Chemical Physics*, 1998, **109**, 8218–8224.

(51) M. E. Casida, C. Jamorski, K. C. Casida and D. R. Salahub, *The Journal of Chemical Physics*, 1998, **108**, 4439–4449.

(52) R. Dennington, T. A. Keith and J. M. Millam, *GaussView Version 5*, Semichem Inc. Shawnee Mission, KS, USA, 2009.